Cell Reports
Medicine

Article

Phylogenomics-driven metalloantibiotic engineering: Overcoming ciprofloxacin resistance in *Pseudomonas aeruginosa* with sideromycin-bismuth synergy

Graphical abstract

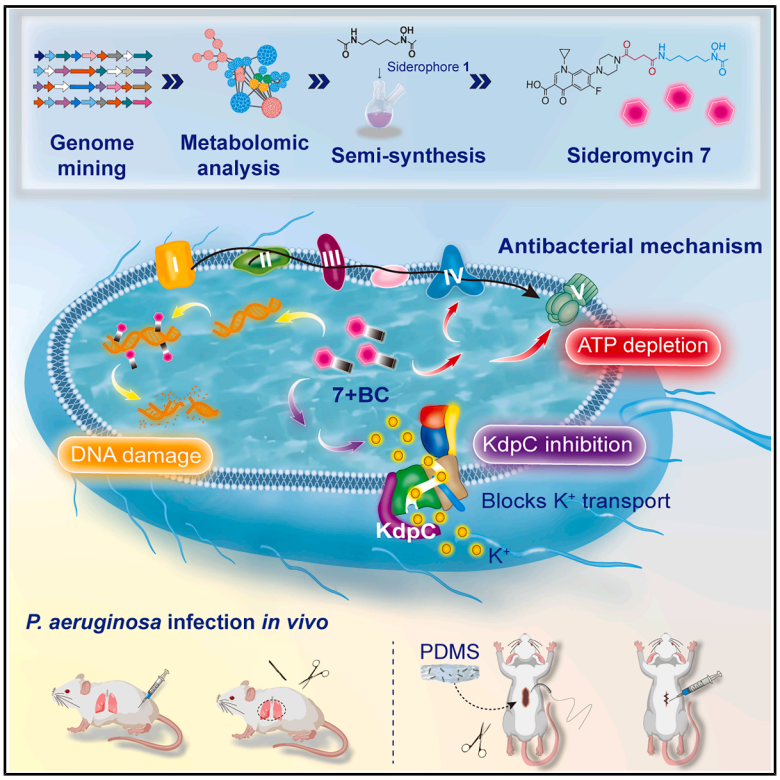

Highlights

- Phylogenomics-driven metalloantibiotic engineering to overcome *P. aeruginosa* resistance
- Sideromycin 7-bismuth features a three-pronged antibacterial mechanism
- The combination of sideromycin 7 and bismuth citrate shows high potency and safety *in vivo*

Authors

Jianwei Chen, Jiangwei Pan, Xingyue Lu, ..., Jianwei Nai, Dahong Zhang, Hong Wang

Correspondence

cjw983617@zjut.edu.cn (J.C.), hongw@zjut.edu.cn (H.W.)

In brief

Chen et al. report a phylogenomics-guided strategy to devise a sideromycin-bismuth metalloantibiotic that overcomes ciprofloxacin resistance in *P. aeruginosa*. The self-assembled complex enters bacteria via iron uptake pathways and exerts three-pronged lethality by disrupting DNA integrity, ATP production, and potassium transport, demonstrating potent *in vivo* efficacy with favorable safety.

Chen et al., 2026, Cell Reports Medicine 7, 102637
March 17, 2026
https://doi.org/10.1016/j.xcrm.2026.102637

CellPress

Cell Reports Medicine

CellPress
OPEN ACCESS

Article

Phylogenomics-driven metalloantibiotic engineering: Overcoming ciprofloxacin resistance in *Pseudomonas aeruginosa* with sideromycin-bismuth synergy

Jianwei Chen,[1,7,8,*] Jiangwei Pan,[1,7] Xingyue Lu,[1,7] Lu Wang,[1,7] Keli Tan,[1] Yujie Yue,[1] Liting Gu,[1] Siqi Wang,[1] Minghong Chen,[2] Hong Jiang,[2] Yu Pan,[3] Yuanquan Yu,[4] Jianwei Nai,[5] Dahong Zhang,[6] and Hong Wang[1,*]

[1]College of Pharmaceutical Science & Jianxing Honors College, Zhejiang University of Technology, Hangzhou 310014, China
[2]Fujian Provincial Key Laboratory of Screening for Novel Microbial Products, Fujian Institute of Microbiology, Fuzhou 350007, China
[3]Institute of Microbiology, Heilongjiang Academy of Sciences, Harbin 150010, Heilongjiang, China
[4]The Second Affiliated Hospital, Zhejiang University School of Medicine, Hangzhou 310003, China
[5]College of Materials Science and Engineering, Zhejiang University of Technology, Hangzhou 310014, China
[6]Urology & Nephrology Center, Department of Urology, Zhejiang Provincial People's Hospital, Affiliated People's Hospital, Hangzhou Medical College, Hangzhou 310014, China
[7]These authors contributed equally
[8]Lead contact
*Correspondence: cjw983617@zjut.edu.cn (J.C.), hongw@zjut.edu.cn (H.W.)
https://doi.org/10.1016/j.xcrm.2026.102637

SUMMARY

Antimicrobial resistance exacerbates the difficulty of clinical bacterial infection treatment, as single-target antibiotics rapidly lose efficacy shortly post-clinical use. Such resistance highlights an urgent need for multi-targeted therapeutics. Metalloantibiotics, combining metal ions with antimicrobials to disrupt diverse bacterial pathways, represent a promising strategy to circumvent resistance. Here, we engineer a sideromycin-bismuth molecular nanoassembly for treating ciprofloxacin-resistant *Pseudomonas aeruginosa*. Using phylogenomics-driven methods, we identify four hydroxamate siderophores from *Streptomyces fradiae* and rationally design sideromycin 7 by a structure-based strategy. Sideromycin 7 forms a 7-Bi^{3+} coordination complex with bismuth citrate, exerting a three-pronged antibacterial mode of action: direct DNA binding to induce damage and arrest replication, suppression of KdpC synthesis to block KdpFABC-mediated potassium transport, and inhibition of ATP production. In murine models, this combination therapy exhibits potent efficacy against ciprofloxacin-resistant *P. aeruginosa* with a considerable safety index. Our findings highlight the potential of phylogenomics-guided metalloantibiotic engineering for overcoming drug resistance.

INTRODUCTION

Antibiotic-resistant bacterial infections pose a growing threat to global health. The stagnation of new antibiotic approvals in recent decades, combined with the widespread misuse and overuse of existing antibiotics, has accelerated the emergence of resistant bacteria.[1,2] The COVID-19 pandemic further strained healthcare systems, impeding efforts to combat antimicrobial resistance effectively.[3] This situation underscores the urgent need for new antimicrobial drugs or innovative strategies to broaden the range of treatment options.

Siderophores are multidentate Fe(III)-binding agents.[4,5] Owing to their ability to bind iron and be readily taken up by microbes, these high-affinity Fe ligands offer a promising strategy to combat antibiotic-resistant pathogenic bacteria. In this approach, siderophores, acting as targeting molecules, can facilitate the delivery of drugs into bacterial cells via active transport pathways, circumventing the membrane barrier.[6] An example of this approach is cefiderocol (Fetroja), a clinically utilized siderophore-antibiotic conjugate (sideromycin) comprising a biscatechol moiety derived from natural siderophores and ceftazidime.[7] Initially approved for the treatment of complicated urinary tract infections in 2019, cefiderocol has shown efficacy in combating challenging infections; however, its reliance on a single mechanism of action presents a vulnerability, which is readily exploited by efflux pumps and target mutations. The emergence of cefiderocol-resistant strains, such as those of *Pseudomonas aeruginosa* and other Gram-negative pathogens, highlights the ongoing challenges associated with antimicrobial resistance.[8,9]

To address this vulnerability, we implement a phylogenomics-guided strategy to mine siderophores for the rational design of next-generation sideromycins. Bioinformatics and omics tools allow us to analyze large datasets, reveal hidden biosynthetic pathways, and identify potential drug candidates that can be missed by traditional methods. This approach highlights the transformative power of gene mining in drug discovery, enabling the identification and optimization of promising compounds. More critically, we propose engineering sideromycins as "metallo-warheads"—dual-function conjugates that integrate iron transport with a cytotoxic metal payload. Bismuth, a "forgotten

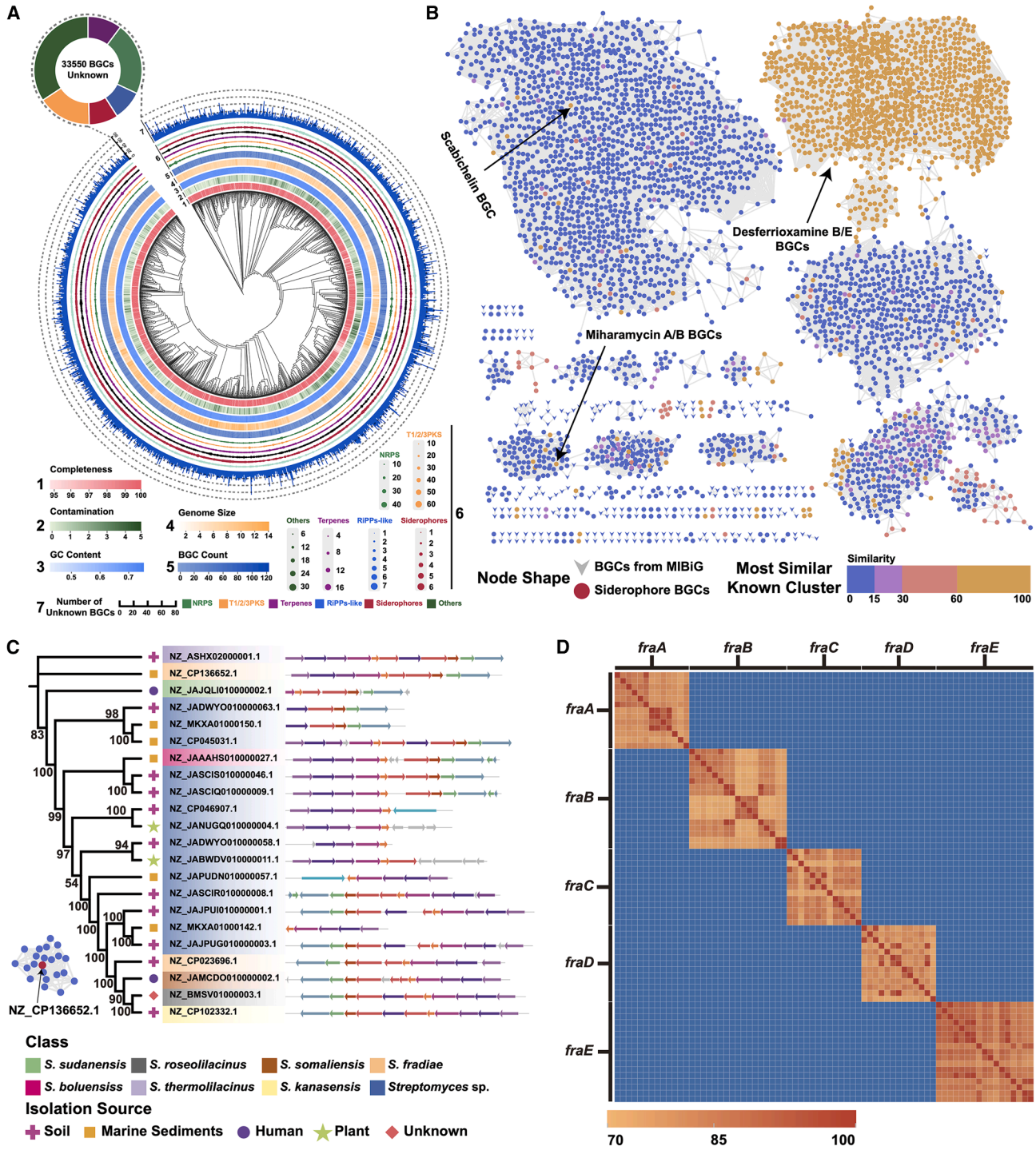

Figure 1. Global analysis of BGCs in *Streptomyces* strains

(A) Construction of a phylogenetic tree for 1,640 *Streptomyces* strains downloaded from NCBI, along with the genomic distribution of all BGCs within these strains. The data representation moves from the outer layer to the inner layer. The outer layers depict the number of unknown BGCs (<15% similarity) and different BGC classes (with circle sizes corresponding to their frequencies). The inner layers indicate the BGC count, genome size, GC content, contamination, and completeness of the genomes.

(legend continued on next page)

warrior'' due to its historical use in antimicrobial therapies (e.g., bismuth subsalicylate for *Helicobacter pylori* infections) and subsequent underutilization in modern medicine, has shown promise as an ideal partner for sideromycins.[10,11] However, the lack of precise delivery systems has hindered its clinical application. We hypothesize that coupling sideromycin to bismuth could enable multimechanistic lethality: the siderophore component facilitates targeted delivery, while bismuth exerts complementary bactericidal effects.

In this study, we designed a sideromycin **7**-bismuth conjugate based on a phylogenomics-driven method and a metallo-warheads strategy; it exhibited remarkable efficacy against ciprofloxacin-resistant *P. aeruginosa* infections both *in vitro* and *in vivo*, while maintaining a favorable safety profile. Sideromycin **7**-bismuth exhibited a three-pronged mechanism: it directly binds to DNA to induce bacterial DNA damage; inhibits K^+ transport by interfering with the formation of KdpFABC complex and high-affinity, ATP-driven K^+ transport; and reduces ATP production. This approach offers valuable perspectives for developing new antibiotics to address the growing challenge posed by drug-resistant pathogens.

RESULTS

Biosynthetic potential of the global *Streptomyces* siderophore biosynthetic gene clusters

To develop an appropriate metalloantibiotic, we initially aimed to identify siderophore biosynthetic gene clusters (BGCs) using a phylogenomic approach. The genome sequences of 3,013 *Streptomyces* strains were downloaded from the National Center for Biotechnology Information (NCBI) (Data S1). We used dRep to remove 1,273 redundant genomes, which resulted in a nonredundant dataset.[12] We then used CheckM[13] to remove 99 strains because of either low completeness of the genome sequence (below 95%) or high contamination (exceeding 5%) (Data S2). The genome sizes ranged from 2.67 to 12.67 Mb, with an average size of 8.19 Mb. We initiated the analysis by employing antiSMASH[14] to predict and annotate the secondary metabolite BGCs in the 1,640 *Streptomyces* strains. A total of 58,090 BGCs were identified and categorized into six classes, exhibiting high diversity (Figure 1A). Type I/II/III polyketide synthases (T1/2/3 PKSs) constituted the most abundant BGC class, accounting for 27.3% of all the BGCs. Nonribosomal peptide synthetases (NRPSs) represented the second largest class, comprising 24.4% of the total BGCs. The abundances of PKS and NRPS BGCs suggest that their products play essential ecological roles. Ribosomally synthesized and post-translationally modified peptides, siderophores, and terpenes accounted for 6.7%, 7.7%, and 16.8% of the total BGCs, respectively, among the *Streptomyces* strains. The ''Others'' group of BGCs comprised various minor classes and hybrid clusters. In the antiSMASH database for gene cluster family (GCF) mining, 57.7% of the *Streptomyces* BGCs were not annotated and had unknown functions (Figure 1A; Data S3, S4, and S5). Hence, *Streptomyces* species hold potential as a valuable source for natural product discovery.

Siderophores were associated with GCFs exhibiting broad phylogenomic distributions and high prevalence, present in 99.7% (1,635/1,640) of the *Streptomyces* strains. This near-universal conservation underscores the critical role of siderophores in microbial adaptation to iron-limited niches across diverse ecosystems. Siderophores are capable of capturing iron from the surrounding environment for the survival of microorganisms. Given the substantial frequency of unidentified BGCs, we investigated the novelty and diversity of siderophore BGCs in all *Streptomyces* strains. To achieve this, we initially compared *Streptomyces* BGCs with the reference BGCs from the Minimum Information about a Biosynthetic Gene Cluster (MIBiG)[15] database, utilizing the Biosynthetic Gene Similarity Clustering and Prospecting Engine (BiG-SCAPE).[16] This approach enabled rapid and interactive analysis of the sequence similarity network among BGCs and GCFs. Among the 2,502 reference BGCs from MIBiG, 248 were identified within the gene cluster network of *Streptomyces* and organized into 146 GCFs. Using antiSMASH, we subsequently attempted to gauge the novelty of siderophore BGCs by comparing each with the most similar known cluster. We established four distinct intervals to evaluate this novelty (Figure 1B). Approximately 29.3% of the siderophore BGCs, highlighted in orange, exhibited >60% similarity, and had been previously identified. However, a majority of the nodes (blue or purple) presented a similarity of less than 30%, indicating that a significant proportion of the siderophore BGCs were underexplored. This finding suggests substantial untapped potential for *Streptomyces* in siderophore biosynthesis, warranting further research.

We selected *Streptomyces fradiae* FIMYZ-003 from laboratory collection and performed antiSMASH analysis, which revealed the presence of two siderophore BGCs in its genome. These two BGCs were subsequently integrated into our in-house siderophore BGC database (Figure 1B) and analyzed using BiG-SCAPE. The results showed that one of the BGCs was identical to the desferrioxamine B/E BGCs (100% similarity) and formed a GCF with other BGCs exhibiting 60%–100% similarity. The other BGC clustered into a GCF with 21 siderophore BGCs but displayed low similarity (<15%), suggesting its potential involvement in the synthesis of previously unreported siderophores (Figure 1C). Phylogenetic tree analysis revealed that these 22 siderophore BGCs were clustered into three clades indicating evolutionary relationships and varying rates of genetic changes (Figure 1C). Each of the core synthetases encoding siderophores was further compared via multiple sequence alignment software,[17] revealing that each synthetase presented greater than 70% identity with the other corresponding proteins from the homologous clusters, indicating a high degree of

(B) BiG-SCAPE analysis of 4,497 siderophore BGCs detected by antiSMASH 6.0 in 1,640 *Streptomyces* strains and comparison with the MIBiG database of reference BGCs. Each node represents a siderophore BGC. Different colors indicate the similarity between siderophore BGCs and the most similar known clusters.

(C) Phylogeny and gene organization of the 22 siderophore BGCs. The construction of the phylogenetic tree is based on the amino acid sequence alignment for the siderophore BGCs.

(D) Each *fra* gene encodes a protein that is more than 70% identical to the corresponding proteins in all 22 clusters.

conservation of siderophore gene clusters in all 22 clusters (Figure 1D; Data S6). Although core genes are usually highly conserved, accessory genes are significantly different, possibly as a result of ecological adaptation to different environments. In microorganisms, every existing BGC is the result of evolution and is tailored to meet microbial growth requirements. These gene clusters and the siderophores they biosynthesize are highly conserved and likely important to the growth and fitness of *Streptomyces* spp. Despite the core genes being widespread and highly conserved among *Streptomyces* spp., the chemical structures of the siderophores produced by the encoded biosynthetic pathways remain to be investigated.

Discovery and putative biosynthetic pathways of siderophores from *S. fradiae*

To validate the chemical novelty predicted by phylogenomics, we further explored as-yet-unknown siderophores from *S. fradiae* FIMYZ-003 by using a building block-based molecular network.[18–20] To activate the expression of siderophore biosynthetic genes, we utilized both solid- and liquid-state fermentation methods. Analysis of ultrahigh-performance liquid chromatography-tandem mass spectrometry (UPLC-MS^2) data led to the detection of 9,054 features. We further correlated these features with the building blocks of siderophores (*m/z* 144.1 ± 14.02, corresponding to the hydroxamate-type siderophore substructure). This strategy (Figure 2A) resulted in the discovery of 4 unreported siderophores (**1**–**4**) and 12 known siderophores (Figures 2A and S1), the structures of which were characterized by high-resolution electrospray ionization tandem mass spectrometry (HRESI-MS^2) (Figure S2). Fraberin (**1**) represents a previously unreported class of hydroxamate siderophores. Fraberin (**1**) was isolated and confirmed by extensive physicochemical and spectroscopic analyses (Figures 2B, S1A, and S3A–S3I; Table S1). Fraberin (**1**) was identified as a siderophore on the basis of its Chrome azurol S activity (Figure S3J).

We conducted further analysis on the functions of enzymes encoded by the siderophore BGC located at positions 4,206,736–4,222,138 on the genome. Among these enzymes, three putative core enzymes—FraA (decarboxylase), FraB (*N*-monooxygenase), and FraD (acyl transferase)—may play crucial roles in the biosynthesis of **1** (Figure 2C). FraA facilitates the decarboxylation reaction from lysine to diaminopentane (DP), FraB catalyzes the conversion of DP to *N*-hydroxy-1,5-diaminopentane (HDP), and FraD facilitates the acetylation reaction from HDP to *N*-acetyl-*N*-hydroxy-1,5-diaminopentane (AHDP). On the basis of the chemical structure, we hypothesize that the conversion from AHDP to fraberin (**1**) occurs spontaneously. To test this hypothesis, we conducted *in vitro* assays, which revealed that the biosynthesis of fraberin from AHDP occurs spontaneously in the presence of acetyl-CoA at 37°C (Figure S4A). Although two siderophore synthetases, FraC and FraE, are not directly involved in the biosynthesis of **1**, fraberin (**1**) is an integral component of the siderophores **2**–**4**. Therefore, we propose that FraC and FraE catalyze the transformation of **1** to **2**–**4**.

Cheminformatics-guided chemical synthesis

We created a virtual database of ciprofloxacin-siderophore conjugates based on **1**–**4** to evaluate the druggability of the sideromycins. In accordance with Lipinski's rule of five,[21] the molecular weights of conjugates based on siderophores **2**–**4** exceeded 750. For conjugates based on siderophore **1**, the molecular weight, number of hydrogen bond acceptors, lipid-water partition coefficient, and number of rotatable bonds were 573, 8, 2.13, and 12, respectively (Tables S2 and S3), thereby exhibiting promising drug-like properties.

To evaluate the effective binding of siderophore **1** to outer membrane proteins of *P. aeruginosa* and to facilitate iron transport, we performed molecular docking studies of **1**-Fe^{3+} and three known Fe^{3+}-containing siderophores (ferrioxamine B, nocardamine, and enterobactin) with 12 outer membrane proteins of *P. aeruginosa*. The optimal conformations of FoxA gave binding affinities of −3.5 kcal/mol with **1**-Fe^{3+}, −11.1 kcal/mol with ferrioxamine B-Fe^{3+}, and −10.9 kcal/mol with nocardamine-Fe^{3+}, while the binding affinity of enterobactin-Fe^{3+} with PfeA was −9.0 kcal/mol (Figures 2D and S5). These results are consistent with previously reported crystal structures of the ferrioxamine B-Fe^{3+}-FoxA,[22] nocardamine-Fe^{3+}-FoxA,[23] and enterobactin-Fe^{3+}-PfeA complexes.[24]

Following the molecular docking studies, molecular dynamics (MD) simulations of the **1**-Fe^{3+}-FoxA complex were performed by using GROMACS with the amber99sb force field.[25–29] The root-mean-square deviation (RMSD) values of the **1**-Fe^{3+}-FoxA complex remained within the range of 0.15–0.3 nm, which indicates stable binding within the complex (Figure 2E). Analysis of the root-mean-square fluctuation (RMSF) results, illustrated in Figure 2F, revealed peaks for residues 773–778, 684–685, 614–615, 518–519, and 385–387, with values ranging from 0.31 to 0.40 Å. These amino acid residues may be located in flexible regions of the protein. However, the generally low magnitude of these fluctuations, however, demonstrates the global stability of the protein structure. Analysis of the radius of gyration (Rg) revealed marginal contraction of the **1**-Fe^{3+}-FoxA complex, as evidenced by a slight decrease in the Rg over the time course of the simulations (Figure 2G). The negligible magnitude of this decrease (∼0.05 nm) signifies a highly stable overall conformation throughout the dynamics. The Gibbs free energy landscape provides insights into protein conformational changes by mapping the RMSD and Rg, thereby revealing the energetic features and transition pathways involved in ligand-receptor interactions.[30] The energy surface displayed a well-defined single-well structure, reflecting a highly concentrated energy distribution. The low-energy region was predominantly localized within PC1(RMSD) = 0.15–0.20 nm and PC2 (Rg) = 2.53–2.56 nm, which corresponded to the global energy minimum. This region represented the most stable conformational state of the system. As PC1 and PC2 deviated from this zone, the energy increased sharply, indicating that substantial energy barriers must be overcome for the system to transition away from the global minimum. The two-dimensional contour projection further illustrated the smooth variation in energy distribution and the existence of local energy barriers (Figure 2H). The RMSD, RMSF, Rg, and Gibbs free energy trajectories of the complexes collectively corroborate the high stability of the **1**-Fe^{3+}-FoxA complex and its ability to mediate Fe^{3+} transport into *P. aeruginosa* cells. Consequently, we selected siderophore **1** and its analogs, together with

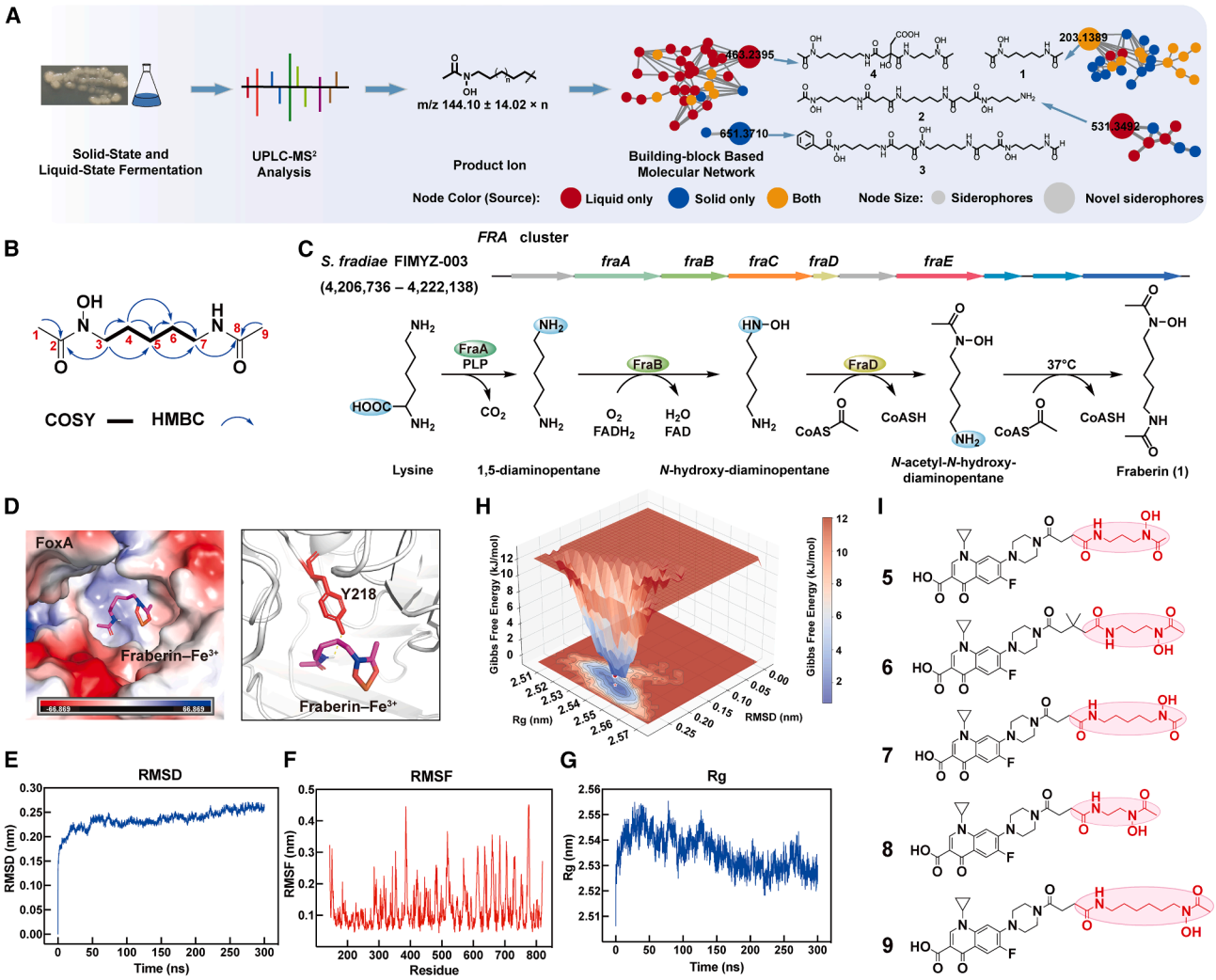

Figure 2. Discovery of fraberin and chemical synthesis of sideromycins 5–9

(A) Diagrammatic workflow for the building block-based molecular network.

(B) Elucidation of the fraberin (**1**) structure.

(C) Detailed and annotated information about the *fra* gene cluster responsible for the biosynthesis of fraberin (**1**).

(D) Predicted binding model for fraberin (**1**)-Fe^{3+} with the FoxA receptor (PDB: 6Z8A).

(E) RMSD of the **1**-Fe^{3+}-FoxA complex (n = 2 technical replicates).

(F) RMSF of the **1**-Fe^{3+}-FoxA complex (n = 2 technical replicates).

(G) Radius of gyration (Rg) curve of the **1**-Fe^{3+}-FoxA complex (n = 2 technical replicates).

(H) Gibbs free energy landscape of the **1**-Fe^{3+}-FoxA complex. The red and blue regions of the free energy landscape indicate high and low free energy states, respectively, with the global minimum marked with a red sphere (3D) and a pentagram (2D) (n = 2 technical replicates).

(I) Chemical structures of sideromycins **5**–**9**.

ciprofloxacin, to synthesize a series of sideromycins **5**–**9** (Figures 2I and S6–S8).

Sideromycins act synergistically with bismuth citrate against ciprofloxacin-resistant *P. aeruginosa*

Building on the rational design of metalloantibiotics, we hypothesized that pairing sideromycins with bismuth citrate could exploit iron uptake pathways to enhance antibacterial efficacy. Historically, metal compounds have served as effective antimicrobial agents, with Bi^{3+} exhibiting cellular uptake similar to that of Fe^{3+}.[31–36] Ranitidine bismuth citrate (Tritec), a combination of ranitidine and bismuth citrate, is a clinically used drug for the treatment of gastric and duodenal ulcers. Its bismuth salts possess anti-*Helicobacter pylori* activity.[37] We tested the effects of cotreatment with sideromycins **5**–**9** with bismuth citrate. Initially, we evaluated the interaction between **5**–**9** and bismuth citrate against ciprofloxacin-resistant *P. aeruginosa* using the standard microdilution checkerboard method. The fractional inhibitory concentration indices (FICIs) were determined to be 0.27–0.5, suggesting the occurrence of a synergistic

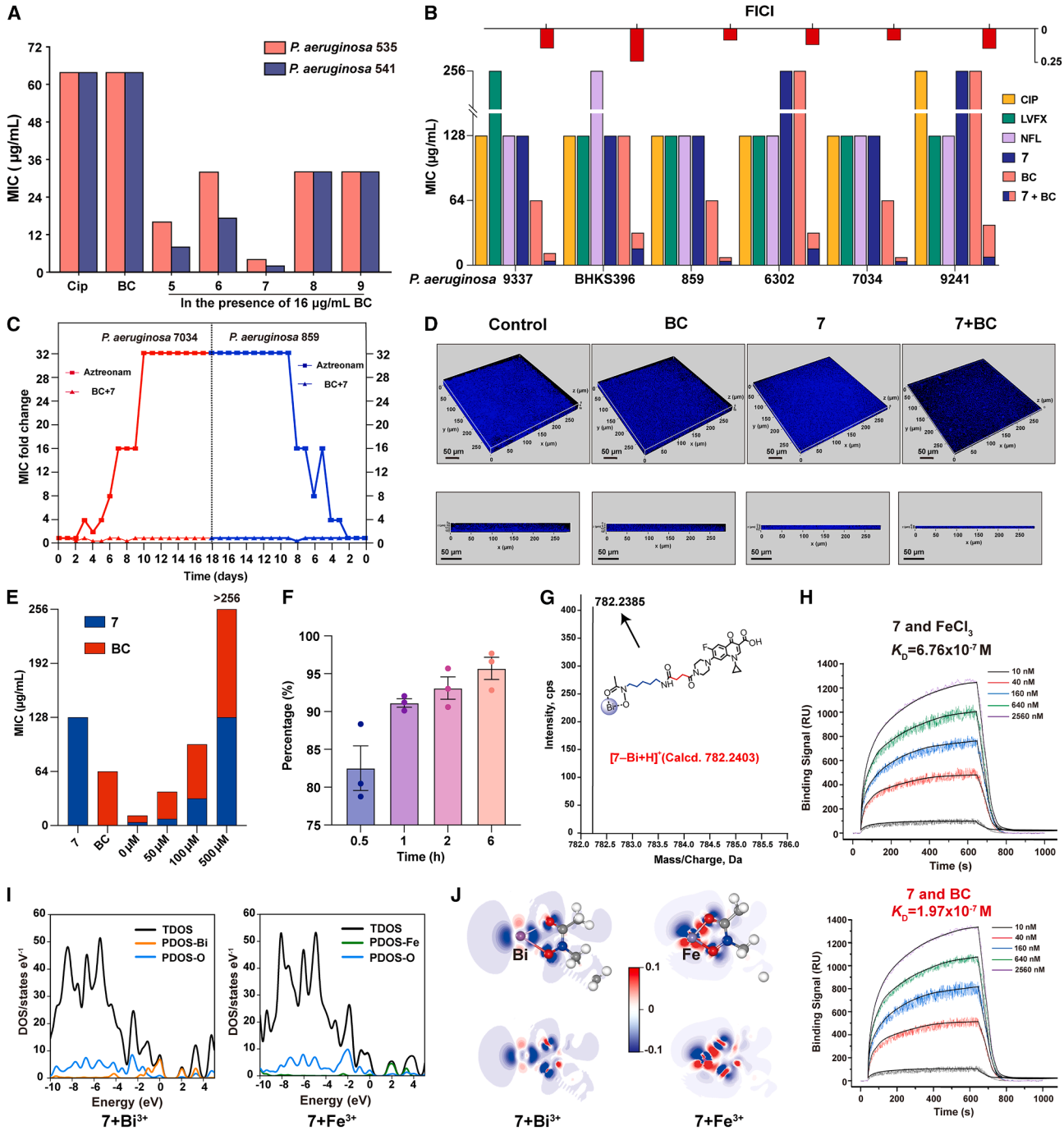

Figure 3. Combination therapy with ciprofloxacin-fraberin conjugates and bismuth citrate against antibiotic-resistant *P. aeruginosa*

(A) Bar chart showing the microdilution checkerboard assay for the combination of bismuth citrate and **5**–**9** against *P. aeruginosa* (n = 3 biological replicates).

(B) MICs of the combination of bismuth citrate and **7** against ciprofloxacin-resistant *P. aeruginosa*. CIP, LVFX, NFL, BC, and **7** were used as controls. The red bar chart (top) shows the FICI values for the combination therapy. CIP, ciprofloxacin; LVFX, levofloxacin; NFL, norfloxacin (n = 3 biological replicates).

(C) Fold increase in the resistance of *P. aeruginosa* 859 and *P. aeruginosa* 7034 to the combination of **7** and bismuth citrate or aztreonam after 18 days of serial passaging with each drug (n = 3 biological replicates).

(D) CLSM images of 3D structures of immature *P. aeruginosa* 541 biofilms treated with bismuth citrate, **7**, or their combination at 4× MIC for 24 h (top, vertical view; bottom, side view). Control: 2% ammonia +5% DMSO.

(E) Effect of Fe^{3+} on the combined bactericidal activity of bismuth citrate and compound **7** against *P. aeruginosa* 9337 (n = 3 biological replicates).

(F) Intracellular bismuth levels in *P. aeruginosa* 541 following treatment with a combination of bismuth citrate and compound **7** compared to bismuth citrate alone (n = 3 biological replicates).

(legend continued on next page)

interaction (FICI≤0.5) between **5**–**9** and bismuth citrate (Figures 3A, S9A, and S9B). The minimum inhibitory concentrations (MICs) of **5**–**9** against *P. aeruginosa* were reduced 4- to 64-fold upon the addition of 16 μg/mL bismuth citrate. The MICs of **5**–**9** combined with bismuth citrate were reduced 1.3- to 7.1-fold compared with those of ciprofloxacin and bismuth citrate alone, with **7** combined with bismuth citrate showing the greatest antibacterial activity against ciprofloxacin-resistant *P. aeruginosa in vitro*. We then examined the efficacy of the combination of **7** and bismuth citrate against six highly ciprofloxacin-resistant *P. aeruginosa* strains (MIC≥128 μg/mL), and synergistic interactions were observed (FICI≤0.25). Compared with those of ciprofloxacin, norfloxacin, and levofloxacin alone, the MICs of the combination therapy with **7** and bismuth citrate were 3.2- to 21-fold lower (Figures 3B and S9C). The synergistic combination of compound **7** with bismuth citrate demonstrated potent antipseudomonal efficacy against ciprofloxacin-resistant *P. aeruginosa* strains *in vitro*, surpassing the antimicrobial performance of conventional quinolone antibiotics. To further assess the antibiotic potential of the combination therapy, we sought to determine the frequency at which bacteria develop resistance to the **7**-bismuth citrate combination. Over an 18-day period, the growth of *P. aeruginosa* 7034 and *P. aeruginosa* 859 remained constant in the presence of the **7**-bismuth citrate combination. In contrast, the MICs of aztreonam for these strains increased by 32-fold (Figure 3C). Confocal laser scanning microscopy (CLSM) was employed to assess the antibiofilm activity of the combination therapy with **7** and bismuth citrate. Our findings revealed that the combined treatment significantly inhibited *P. aeruginosa* biofilm formation, achieving 78% reduction at 4× MIC compared with the control. In contrast, bismuth citrate alone exhibited no discernible antibiofilm activity. While **7** alone displayed antibiofilm capacity, biofilm formation decreased by 44% in the combined treatment group, indicating a synergistic interaction. These results underscore the potent antibiofilm activity of the combination of **7** and bismuth citrate (Figure 3D).

Bi^{3+} chelate of compound 7 targets ATP, DNA, and K^+ transport

The combination of sideromycin **7** and bismuth citrate is an appealing candidate antibiotic; however, elucidating its mechanism of action (MOA) is a significant challenge. To obtain further mechanistic insight into the synergistic effect of sideromycin **7** and bismuth citrate, we examined whether Fe^{3+}can alter the synergistic bactericidal effect. A checkerboard microdilution assay revealed a striking Fe^{3+}-dependent attenuation of the synergistic bactericidal effect between bismuth citrate and **7** against *P. aeruginosa*. In the absence of Fe^{3+}, a strong synergy was observed, with a FICI of 0.156. This synergy was progressively diminished by the addition of exogenous Fe^{3+}, as evidenced by an increased FICI of 0.313 at with 50 μM Fe^{3+}, the transition to a merely additive effect at 100 μM Fe^{3+} (FICI of 0.75), and ultimately abrogation of bactericidal effects upon treatment with 500 μM Fe^{3+} (Figures 3E and S9D). Moreover, as illustrated in Figure 3F, compared with bismuth citrate alone, combination treatment resulted in increased intracellular bismuth levels. These results confirm that the synergistic bactericidal effect is mediated by iron homeostasis-dependent bismuth uptake. We further examined whether sideromycin **7** binds to Bi^{3+}. Compared with that in the presence of bismuth citrate alone, the transport of Bi^{3+} from bismuth citrate into *P. aeruginosa* cells increased in the presence of sideromycin **7** and bismuth citrate, as evidenced by inductively coupled plasma mass spectrometry (ICP-MS) (Figure 3F). In addition, after incubation of bismuth citrate with **7**, a new peak in the HRESI-MS appeared at 782.2385 and was assigned as [**7**-Bi+H]$^+$ (calculated. 782.2403) by HRESI-MS (Figure 3G). These findings suggested the formation of a **7**-Bi^{3+} complex and a chelation ratio of 1:1 between sideromycin **7** and Bi^{3+}. We also observed a significant binding affinity between **7** and bismuth citrate, with a K_D value of 197 nM. **7** exhibited a greater binding affinity for bismuth citrate than $FeCl_3$ (K_D = 676 nM) (Figure 3H). The binding energy (Eb) calculations indicated that sideromycin **7** had a substantially stronger affinity for Bi^{3+} (−4.17 eV) than for Fe^{3+} (−3.17 eV), which was consistent with the measured binding affinities. Density of states analysis revealed that the total density of states (TDOS) near the Fermi level in the **7**-Bi complex could be attributed primarily to Bi and O orbitals, suggesting significant orbital hybridization between Bi and O atoms. In contrast, such hybridization was not observed in the **7**-Fe complex (Figure 3I). Additionally, the band gap of the **7**-Bi system was larger than that of the **7**-Fe system. These results indicate that the **7**-Bi system has a more stable electronic structure, making it more difficult for electrons to transition from the valence band to the conduction band. The charge density difference (CDD) further confirms that the **7**-Bi system has a greater number of electrons being transferred from Bi^{3+} to sideromycin **7**, resulting in stronger interactions (Figure 3J). These findings indicate that when sideromycin **7** is mixed with Bi^{3+} and injected into the body, it preferentially binds Bi^{3+} to form a stable complex, which reduces the opportunity for sideromycin **7** to bind Fe^{3+}, inhibits the uptake of iron by bacteria, and promotes bismuth accumulation by *P. aeruginosa*. This highlights the promising role of the sideromycin-bismuth complex assembly formed by chelating bismuth ions with sideromycin in the development of novel antimicrobial therapies and underscores the importance of metal-ligand interactions in biomedical research.

The binding of bismuth to **7** suggests that bismuth and ciprofloxacin might use *P. aeruginosa*'s iron delivery system for internalization and accumulation. To gain insight into potential targets, we used scanning electron microscopy (SEM) (Figure 4A)

(G) HRESI-MS spectrum of the bismuth conjugate of compound **7**.
(H) SPR showed the dissociation constant (K_D) for the interaction between **7** and $FeCl_3$ as well as **7** and BC.
(I) TDOS and partial density of states (PDOS) for **7**+Bi^{3+} and **7**+Fe^{3+}. The TDOS near the Fermi level reveals a key difference: the TDOS is dominated by Bi–O orbital hybridization in the **7**+Bi^{3+} system but shows no such dominance from Fe–O hybridization in the **7**+Fe^{3+} system.
(J) CDD maps of the **7**+Bi^{3+} and **7**+Fe^{3+} systems. The red regions indicate charge accumulation, whereas the blue regions indicate charge depletion. BC, bismuth citrate.

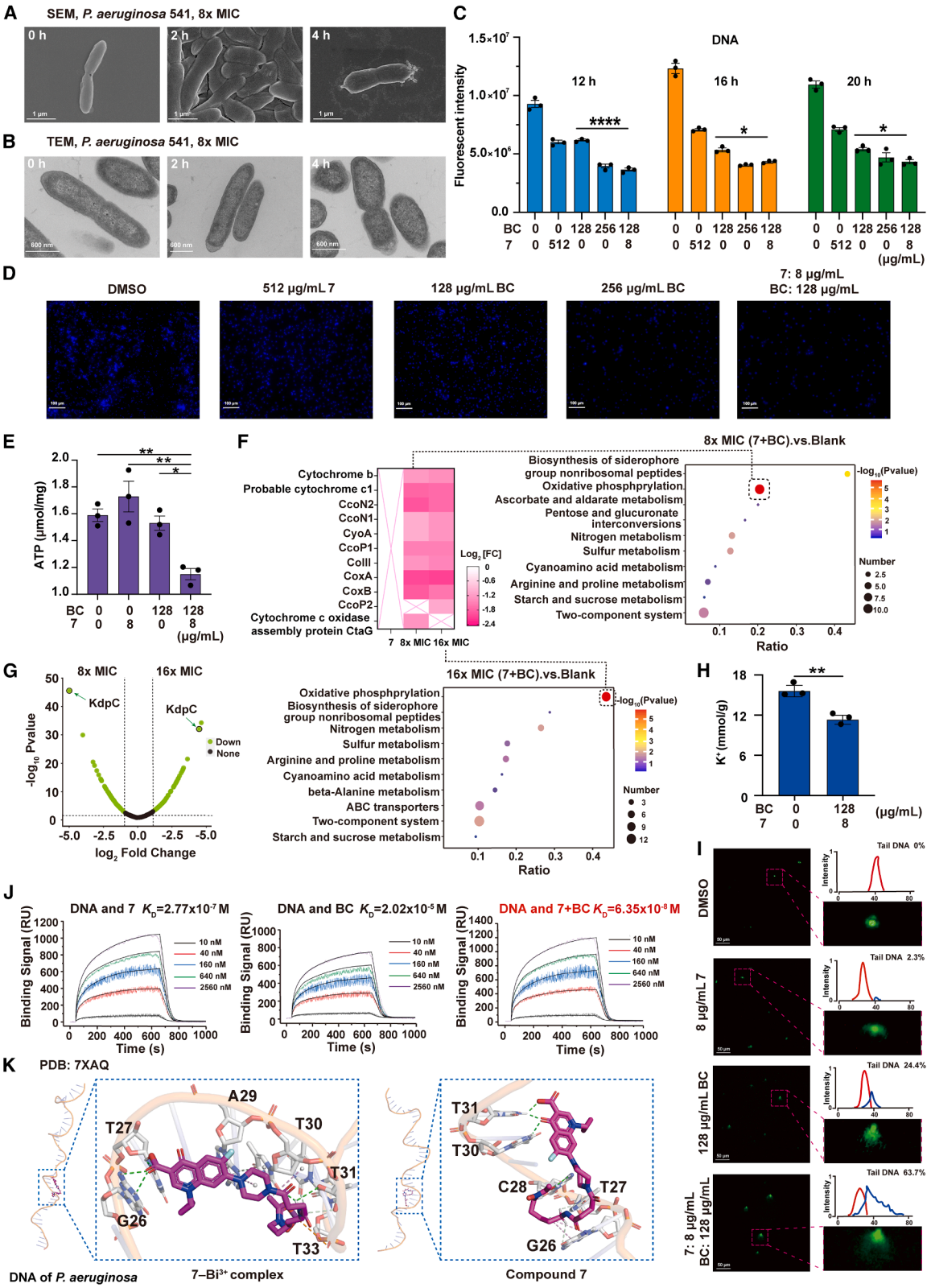

(legend on next page)

and transmission electron microscopy (TEM) (Figure 4B) to observe morphological changes in *P. aeruginosa* cells subjected to combined treatment (8× MIC for 0, 2, or 4 h). We noted time-dependent deformation (Figures S10A and S10B); at higher concentrations, the cells displayed spiky projections or leakage of the intracellular contents. However, the cell membrane remained intact, suggesting potential alterations in cell content and ion channels. To identify the specific cellular components affected by the combined therapy, we conducted four experiments including membrane integrity assay, membrane depolarization assay, ATP detection assay, and DNA damage assay. We did not observe an increase in fluorescence intensity with the membrane-impermeable probe propidium iodide or the membrane depolarization-sensitive probe 3,3′-dipropylthiadicarbocyanine iodide [$DiSC_3(5)$], thereby ruling out membrane disruption as the MOA (Figures S10C and S10D); this finding is consistent with the SEM and TEM observations. However, we detected decreased fluorescence intensity with the DNA disruption probe 4′,6-diamidino-2-phenylindole (DAPI) and decreased ATP production, indicating that the combination of sideromycin **7** and bismuth citrate can compromise DNA integrity and replication and disrupt ATP formation (Figures 4C–4E).

To further elucidate the interplay between the **7**-bismuth citrate complex and ATP formation, we measured intracellular reactive oxygen species (ROS) levels in bacteria. Given that ROS are often associated with impaired oxidative phosphorylation and reduced ATP production, we anticipated changes in ROS levels if the complex affected ATP synthesis through this pathway. However, the combined treatment with **7** and bismuth citrate did not induce significant alterations in fluorescence intensity, thereby ruling out a significant role for ROS in the observed ATP depletion (Figure S10E). Subsequently, differential proteomics analysis was performed. The results revealed decreases in the levels of ≥10 proteins associated with oxidative phosphorylation complexes IV and V, directly demonstrating that the **7**-bismuth citrate complex affects the biosynthesis of complexes IV and V to inhibit ATP production (Figures 4F and S10F). Unlike ROS-mediated mechanisms, the complex targets respiratory complexes IV and V, simultaneously reducing ATP production. This direct blockade of electron transport leads to rapid metabolic collapse without inducing oxidative stress. Moreover, differential proteomics analysis revealed selective downregulation of KdpC (a subunit of the K^+-translocating KdpFABC complex[38]), with $\log_2$ 5.0- and 4.2-fold decreases observed in the presence of 8× MIC and 16× MIC **7**-bismuth citrate, respectively (Figure 4G). In contrast, sideromycin **7** alone induced a minimal change, corresponding to a $\log_2$ 0.46-fold increase (Figure S10G). These findings collectively indicate that the **7**-bismuth citrate complex can inhibit the K^+ transport system. This prevented potassium ions from being transported into the cells, leading to an imbalance in the cellular osmotic pressure and causing dehydration. This finding was confirmed by the data presented in Figure 4H, which show that potassium ion levels were significantly reduced in *P. aeruginosa* cells following combined treatment with **7** and bismuth citrate. Furthermore, this result was consistent with the TEM results (Figure 4B), indicating that this osmotic shock bypasses traditional membrane disruption, preserving membrane integrity.

Considering that **7**-bismuth citrate can not only disrupt ATP formation and the K^+ transport system but also lead to DNA damage, we further investigated the interaction between **7**-bismuth citrate and DNA. In the assessment of DNA damage using the neutral comet assay, **7**-bismuth citrate caused more severe DNA double-strand breaks (tail DNA 63.7%) than did **7** (tail DNA 2.3%) or bismuth citrate (tail DNA 24.4%) alone (Figure 4I). Fluorescence spectroscopy showed a regular increase in emission at 467 nm upon titration with the addition of **7** and bismuth citrate. This fluorescence signal was significantly more intense than that induced by compound **7** or bismuth citrate alone, suggesting compound **7** and bismuth citrate may form a complex *in situ*, thereby altering their mode of interaction with DNA (Figure S10H). Subsequently, surface plasmon resonance (SPR) was used to determine the dissociation constants (K_D values) between different samples and *P. aeruginosa* DNA. The results showed that the DNA had a greater affinity for the compound **7** and bismuth citrate mixture (K_D = 63.5 nM) than for compound **7** alone (K_D = 277 nM) or bismuth citrate alone (K_D = 20.2 μM) (Figure 4J). Collectively, the fluorescence measurements and SPR results suggest the complex formed between compound **7** and bismuth citrate may result in

Figure 4. Bactericidal mechanism of the combination of bismuth citrate and 7

(A) SEM image of *P. aeruginosa* 541 cultures treated with the combination of BC and **7** at 8× MIC for 0, 2, or 4 h.

(B) TEM image of *P. aeruginosa* 541 cultures treated with the combination of BC and **7** at 8× MIC for 0, 2, or 4 h.

(C) DNA content of *P. aeruginosa* 541 cultures treated with the combination of BC and **7** at 12, 16, and 20 h. BC and **7** were used alone as controls (n = 3 biological replicates). Mean ± standard error of the mean (error bars) is shown.

(D) DNA fluorescence of *P. aeruginosa* 541 treated with BC, **7** or their combination at 8× MIC for 12 h. Blue fluorescent dots represent bacterial DNA.

(E) ATP content in *P. aeruginosa* 541 treated with BC, **7**, or their combination at 8× MIC for 2 h (n = 3 biological replicates). Mean ± standard error of the mean (error bars) is shown.

(F) Proteomic analysis was performed on *P. aeruginosa* 541 cells grown for 12 h, with or without the combination of **7** and BC (8× MIC and 16× MIC). Scatterplot of the Kyoto Encyclopedia of Genes and Genomes (KEGG) pathways enriched in the downregulated genes and a heatmap (pink) of various downregulated proteins involved in oxidative phosphorylation.

(G) Volcano map of downregulated proteins upon treatment with the combination of **7** and BC (8× MIC and 16× MIC).

(H) Potassium ion assay in *P. aeruginosa* 541 (n = 3 biological replicates).

(I) DNA damage was assessed using a bacterial DNA damage comet assay kit. From the top to the bottom, cells were treated with DMSO, 8 μg/mL **7**, 128 μg/mL BC, and 8 μg/mL **7** + 128 μg/mL BC. The fluorescence intensity of the comet tail indicates DNA damage. Red curve, head DNA%; blue curve, tail DNA%.

(J) SPR was used to determine the dissociation constant (K_D) for the interaction in each group. Genomic DNA was obtained from *P. aeruginosa* 541.

(K) Molecular docking results for the **7**-Bi and **7** with *P. aeruginosa* DNA (PDB: 7XAQ). Green indicates hydrogen bonds, light green indicates C–H bonds, pink indicates hydrophobic interactions, orange indicates electrostatic interactions, and gray indicates metal-acceptor bonds. BC, bismuth citrate.

Statistical comparisons were performed via one-way ANOVA and Dunnett's multiple comparison test (C, E, and H). $^*p < 0.05$, $^{**}p < 0.01$, $^{****}p < 0.0001$.

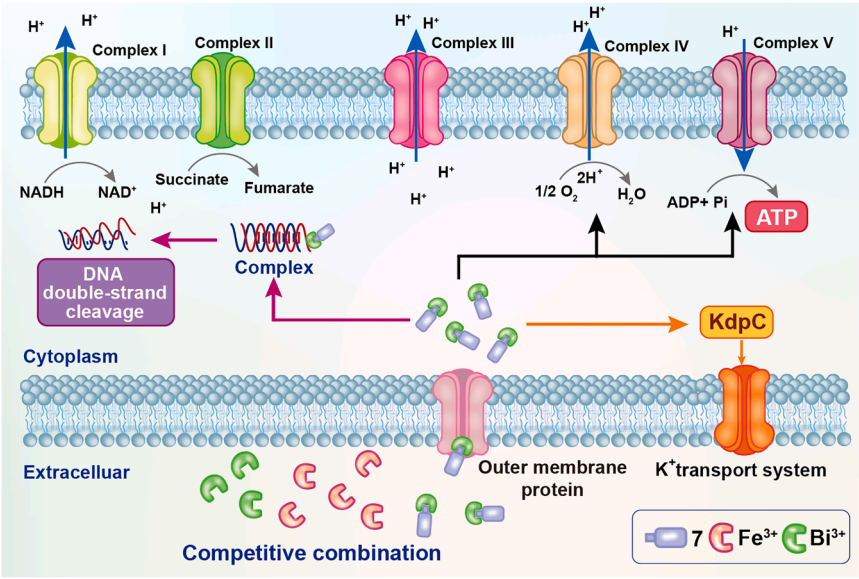

Figure 5. Bactericidal mechanism of the combination of 7 and bismuth citrate

enhanced DNA binding relative to either individual agent alone. Molecular docking revealed the potential binding mechanism of the combination of compound **7** and bismuth citrate with DNA in which Bi^{3+} adopts a pentadentate binding mode, coordinating with one siderophore hydroxamate to form a **7**-Bi complex. Molecular docking revealed that the compound **7**-Bi complex formed five hydrogen bonds, three C–H bonds, three hydrophobic interactions, and an electrostatic interaction (−6.8 kcal/mol) with DNA. This complex interaction network highlights the robust and versatile binding capacity of Bi^{3+} within the DNA structure. In contrast, the docking results for compound **7** alone with DNA revealed the formation of only four hydrogen bonds, three C–H bonds, and two hydrophobic interactions (−5.7 kcal/mol), indicating a comparatively simpler interaction pattern (Figure 4K). These findings underscore the superior binding affinity and intricate coordination chemistry of the Bi^{3+} complex while also demonstrating the relatively limited interaction capabilities of compound **7** with DNA.

Collectively, our findings demonstrate that sideromycin **7** has a strong ability to chelate with Bi^{3+} rather than with Fe^{3+}, thereby facilitating the formation of the **7**-bismuth complex. This complex effectively restores the susceptibility of ciprofloxacin-resistant *P. aeruginosa*, which is achieved through a three-pronged mechanism, involving DNA disruption, interference with the K^+ transport system, and inhibition of ATP production (Figure 5).

The combination of sideromycin 7 and bismuth citrate shows high potency and safety *in vivo*

Given the strong *in vitro* effect of the combination of sideromycin **7** and bismuth citrate, we further investigated their therapeutic potential *in vivo*. We evaluated the *in vivo* antibacterial efficacy of the combination of **7** and bismuth citrate in the mouse model with implanted *P. aeruginosa* biofilm (Figure 6A). After 4 days, the residual *P. aeruginosa* colonies on the biofilms were evaluated by removing the implanted polydimethylsiloxane (PDMS) sheets. Compared with monotherapy, treatment with 8 mg/kg **7** in combination with 8 mg/kg bismuth citrate resulted in a more than 700-fold decrease in the bacterial burden (Figures 6B and 6C). The mice treated with the combination exhibited well-healed wounds without visible inflammation, and the therapeutic effect in these mice was significantly better than that in mice treated with ciprofloxacin, tobramycin, bismuth citrate, or **7** alone (Figures 6D and 6E). Hematoxylin and eosin (H&E) staining revealed decreased necrotic areas and inflammatory infiltrates in skin tissue (Figure 6F) and muscle tissue (Figure 6G) after treatment with **7** in combination with bismuth citrate. However, a high degree of inflammatory infiltration was observed in vehicle-, bismuth citrate-, ciprofloxacin-, or tobramycin-treated mice. We also evaluated the antibacterial potency of the combination therapy in a mouse lung *P. aeruginosa* infection model (Figure 7A). Significant decreases in bacterial abundance in the infected lung tissue were observed in the mice treated with the combination of **7** and bismuth citrate but not in the groups receiving the monotherapies (Figures 7B and 7C). H&E staining demonstrated that, compared with both the monotherapy and model control groups, the combination treatment group exhibited a significant reduction in inflammatory cell infiltration within lung tissues. Notably, the combination therapy group showed marked pathological improvements that closely paralleled those observed in healthy control specimens. These findings confirm that the synergistic interaction between therapeutic agents effectively attenuates post-infectious inflammatory responses while facilitating functional restoration of pulmonary architecture (Figure 7D). In the *P. aeruginosa* killing model, the mice treated with the combination of **7** and bismuth citrate presented strikingly increased survival rates at 168 h after infection (Figure 7E). These results showed that sideromycin **7** exhibited significant synergy with bismuth citrate against ciprofloxacin-resistant *P. aeruginosa*. The *in vitro* activity of the **7**-bismuth citrate combination therapy translated well into efficacy *in vivo*.

Encouraged by the superior performance of the combination of **7** with bismuth citrate in terms of *in vitro* and *in vivo* efficacy, we proceeded to examine its *in vivo* cytotoxicity. The combination appeared to be relatively nontoxic, showing no detectable toxicity in the heart, liver, spleen or kidneys of mice at therapeutic doses (Figures 7F and 7G). Acute toxicity testing in mice revealed that intraperitoneal injection of **7** at a dose of 781 mg/kg did not result in death. Additionally, continuous administration of **7** for 28 days at a maximum dose of 32 mg/kg via intraperitoneal injection resulted in no abnormalities in body weight, blood parameters, or organs

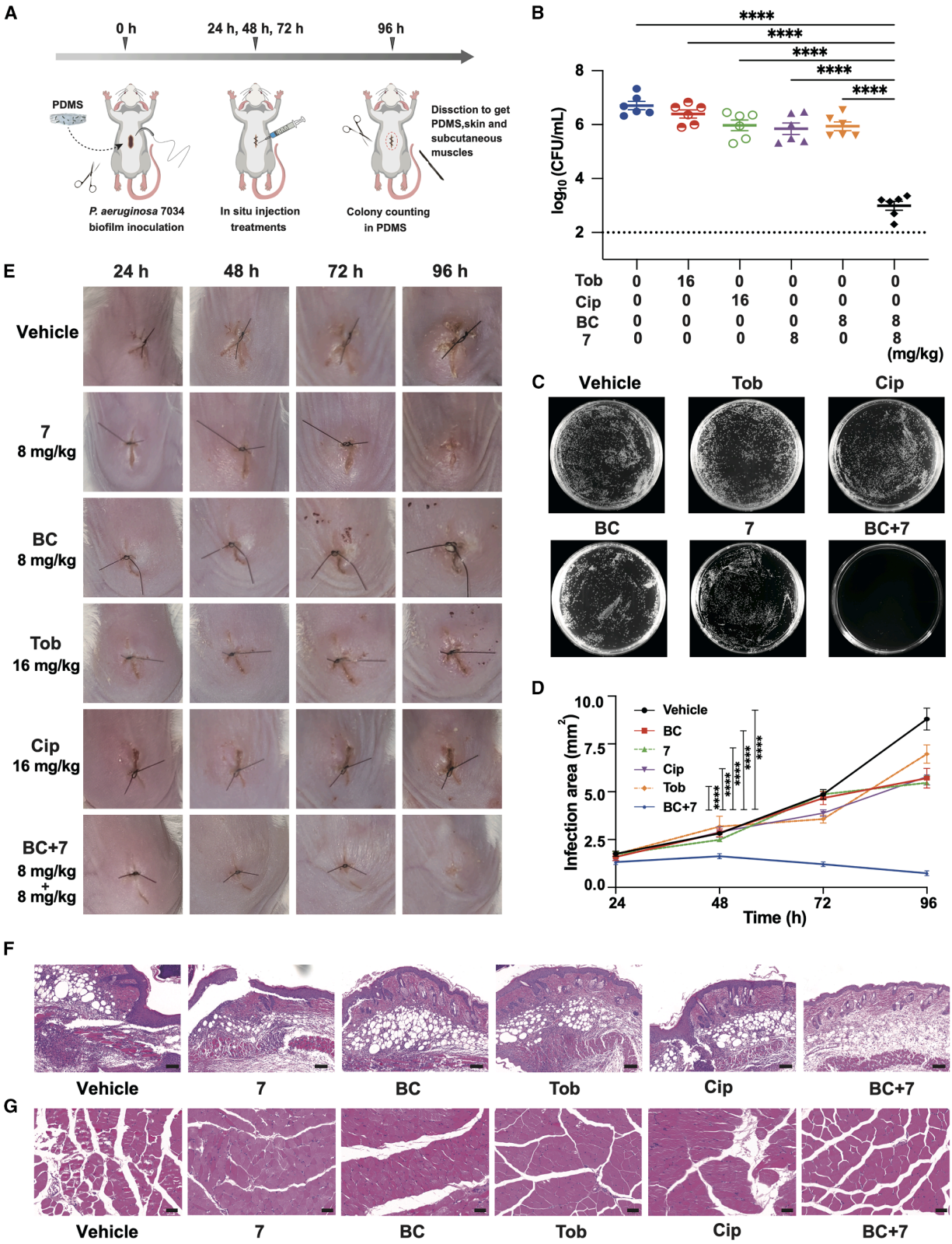

(legend on next page)

(Figure S11; Tables S4 and S5). Additionally, analysis of the cecal contents of the mice revealed no significant differences ($p > 0.05$) in the Chao1 index, observed feature index, Shannon index, Simpson index, principal coordinate analysis results, or species composition at the phylum level among the treatment groups. These findings suggest that continuous administration of compound **7** for 28 days did not lead to significant changes in the structure of the gut microbiota and had no notable effect on its composition or diversity (Figure S12). Collectively, these results indicate that the combination of **7** with bismuth citrate is a relatively safe option as an *in vivo* antibacterial treatment.

DISCUSSION

The emergence and swift dissemination of antimicrobial resistance present a formidable and escalating threat to global public health. This resistance highlights the urgent need for developing novel antibiotics with multiple targets that address bacterial resistance. We propose a phylogenomics-guided design of a sideromycin-metal complex to overcome bacterial resistance. The designed sideromycin **7**, in combination with bismuth citrate, exhibited a three-pronged antibacterial mode of action and demonstrated remarkable efficacy against ciprofloxacin-resistant *P. aeruginosa* infections both *in vitro* and *in vivo*, while maintaining a favorable safety profile.

The discovery of siderophore **1** and its successful application in drug design highlights the untapped potential of natural product mining in the era of genomics. Our analysis extended beyond gene identification to include characterization of gene products, investigation of their interactions with bacterial cells, and examination of the evolutionary pressures driving their biosynthesis. For example, we found that the adaptation of *Streptomyces* to competitive, resource-scarce environments significantly influenced the evolution of the BGCs responsible for producing highly effective siderophores. Despite evolutionary diversification within the genus *Streptomyces*, the function of siderophores has been consistently preserved, suggesting that siderophores play a crucial role in the ecological niche of these bacteria. Analysis of *Streptomyces* genome evolution, characterized by gene loss and gain over time, revealed that the BGC content reflects adaptation through natural selection. Our findings establish a clear link between specific genes and siderophore production in *Streptomyces* and pave the way for the use of siderophore-mediated interactions as a potential tool for the design of new antibiotics to combat drug-resistant pathogens.

Unlike sequential target inhibition, the strategy utilized by our complex is a convergent multimechanistic engagement, inspired by cancer kinase inhibitors.[39] Fraberin (**1**) acts as a "molecular glue" to link bismuth and ciprofloxacin, enabling simultaneous DNA binding and ATP and K^+ transport inhibition. This three-pronged attack raises the evolutionary barrier for resistance: compensatory mutations would require concurrent alterations in DNA, potassium transport, and cytochrome systems—a highly improbable scenario. This result was confirmed by the MIC fold change over 18 consecutive days (Figure 3C).

Our strategy aligns with the growing interest in bismuth-based antimicrobials.[40] This alignment is rooted in a critical common mechanism of the facilitated intracellular delivery of Bi^{3+}, which subsequently imparts potent antibacterial action, particularly in disrupting biofilms. These collective findings position bismuth as a pivotal entity for achieving biofilm eradication. Furthermore, its efficacy can be understood within the context of nutritional immunity—the host's defense by depriving pathogens of iron.[41] To overcome this defense, *P. aeruginosa* employs siderophores for iron acquisition. Bismuth disrupts this iron homeostasis by interacting with these siderophores and the ferric uptake regulator (Fur), thereby impairing iron uptake, inducing intracellular iron deprivation, and ultimately causing bacterial death.[42] Consistent with this mechanism, our data demonstrate that the synergy between sideromycin **7** and bismuth citrate is progressively antagonized by increasing iron levels (Figure 3E), confirming that restored iron homeostasis can abolish the synergistic effect of bismuth.

In addition, the mechanism of DNA damage highlights the crucial role of the five-membered ring formed between bismuth ions and sideromycin **7**. This structural modification dramatically improved the stability of the sideromycin-bismuth-DNA complex, leading to enhanced biological activity. The ring prevents premature dissociation of the compound from DNA and promotes stronger intercalation, thereby increasing the ability of the compound to inhibit *P. aeruginosa* replication by directly interacting with its genetic material. This discovery underscores the effectiveness of incorporating such ring structures in sideromycin design to improve both drug stability and potency. The strength and duration of drug-target interactions are often critical limitations in drug development, particularly when complex molecules such as DNA are targeted. Stabilizing this interaction not only enhances efficacy but also reduces the likelihood of resistance development, as bacteria require multiple adaptive mechanisms to overcome this strengthened binding.

In conclusion, we successfully developed and validated a self-assembled sideromycin-bismuth chelate and demonstrated its potent antipseudomonal efficacy *in vitro* and *in vivo*. Our approach integrates evolutionary genomics, rational drug

Figure 6. *In vivo* potency against an implanted ciprofloxacin-resistant *P. aeruginosa* 7034 biofilm in an animal model

(A) Scheme of the experimental protocol for the animal model with *P. aeruginosa* 7034 biofilm implantation.

(B) Colony count for residual *P. aeruginosa* colonies on the implanted PDMS sheets ($n = 6$ animals). Mean ± standard error of the mean (error bars) is shown. Statistical comparisons were performed by using one-way ANOVA and Dunnett's multiple comparisons test. ****$p < 0.0001$.

(C) Photographs of colonies on agar plates.

(D) The wound areas of the mice were calculated via ImageJ for 4 days ($n = 6$ animals). Mean ± standard error of the mean (error bars) is shown. Statistical comparisons were performed via simple survival analysis (Kaplan-Meier). ****$p < 0.0001$.

(E) Photographs showing the appearance of the wounds at different time points.

(F) H&E staining of the skin of infected mice subjected to different treatments. Scale bars represent 200 μm.

(G) H&E staining of the muscle of infected mice subjected to different treatments. Scale bars represent 200 μm. Cip, ciprofloxacin; Tob, tobramycin; BC, bismuth citrate; vehicle, physiological saline.

CellPress
OPEN ACCESS

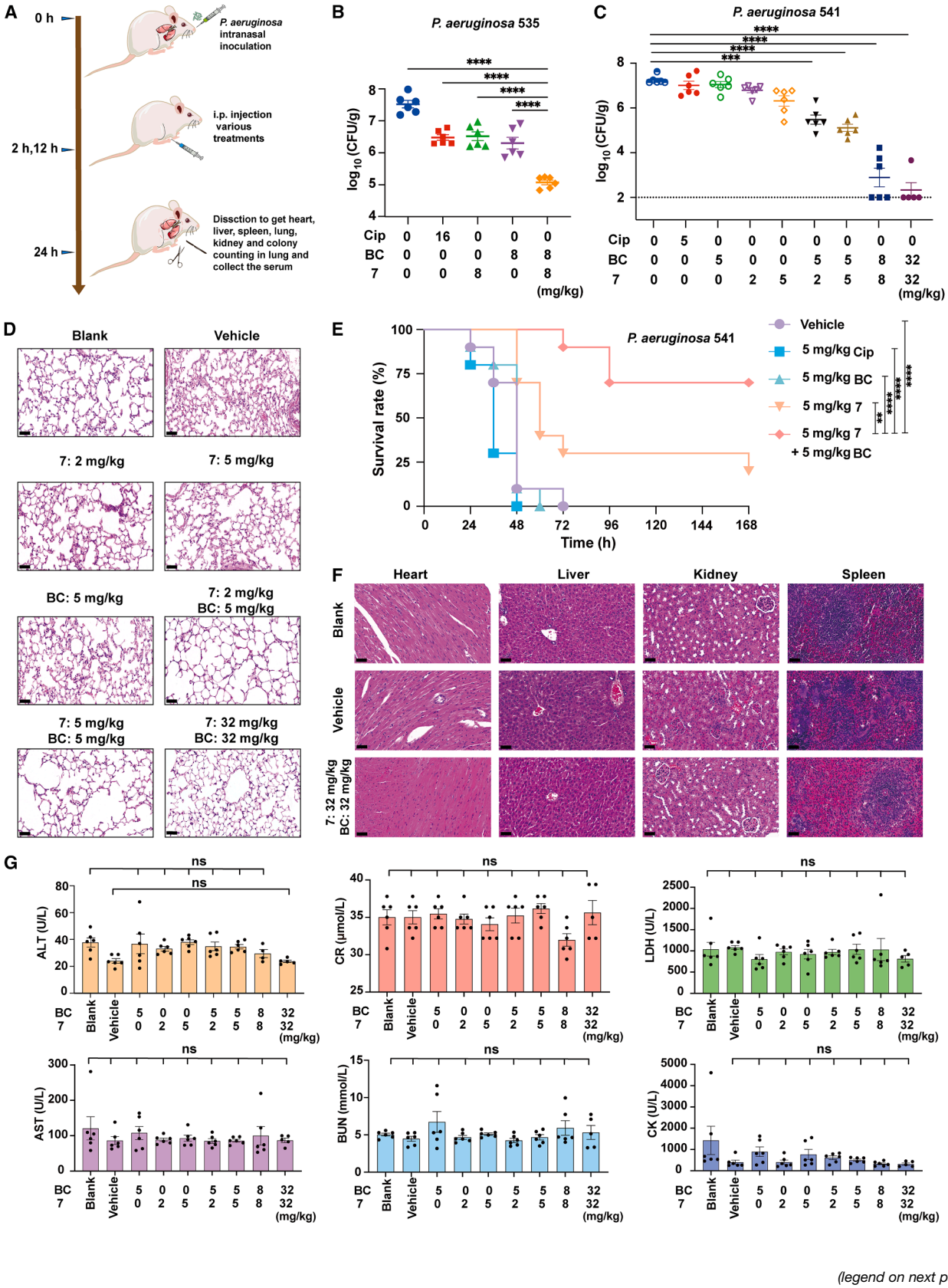

(legend on next page)

design, and multitarget MOAs to address two critical gaps: (1) the lack of sideromycins with multimodal mechanisms and (2) the unmet need for precision delivery systems to harness bismuth's antimicrobial potential. By combining active transport with metalloantibiotic toxicity, this approach not only overcomes the delivery challenges associated with traditional metal-based antibiotics but also provides a paradigm for resistance management using a multitarget "lockdown" strategy.

Limitations of the study

In this study, a self-adaptive sideromycin-bismuth complex for treating ciprofloxacin-resistant *P. aeruginosa* was developed. Although the complex showed strong antipseudomonal efficacy in murine pneumonia and skin infection models, further evaluation in different patient-derived *P. aeruginosa* infection models would provide a more valuable reference for clinical translation. Moreover, we are aware that the systematic biosafety evaluation in the host was limited in this study. In addition, different modes of administration of sideromycin **7** and bismuth citrate should be considered to align with clinical scenarios.

RESOURCE AVAILABILITY

Lead contact

Further information and requests for resources and reagents should be directed to and will be fulfilled by the lead contact, Jianwei Chen (cjw983617@zjut.edu.cn).

Materials availability

All unique and stable reagents generated in this study are available from the lead contact with a completed materials transfer agreement.

Data and code availability

- The authors declare that the main data supporting the results of this study are available within the paper and its supplemental information.
- The mass spectrometry proteomics data generated in this study have been deposited to the ProteomeXchange Consortium via the PRIDE partner repository with the dataset identifiers PXD070105 and PXD069942 (link: https://www.ebi.ac.uk/pride/archive/projects/PXD070105; https://www.ebi.ac.uk/pride/archive/projects/PXD069942).
- The authors developed a Python script to automatically extract detailed information on secondary metabolite gene clusters from antiSMASH predictions. The related code has been uploaded as a "Source Code" resource at Zenodo (https://doi.org/10.5281/zenodo.18213340) to ensure reproducibility.
- Any additional information required to reanalyze the data reported in this paper is available from the lead contact upon request.
- All data reported in this paper will be shared by the lead contact upon request.

ACKNOWLEDGMENTS

This work was financially supported by the Project of International Cooperation and Exchanges NSFC-ASRT (no. W2412100) and National Natural Science Foundation of China (no. 82574317 and 42276137). We gratefully acknowledge platform support from Zhejiang-Egypt Joint Laboratory on Intelligent Discovery of Marine Drugs, Zhejiang International Sci-Tech Cooperation Base of Development and Utilization of Nature Products, Zhejiang Key Laboratory of Green, and Low-carbon and Efficient Development of Marine Fishery Resources.

AUTHOR CONTRIBUTIONS

Projects design, J.C. and H.W.; genome and biosynthetic gene cluster, MS^2 data, and biosynthetic pathway study, J.P., X.L., and Y. Yue; *in vivo* and *in vitro* experiments and model of action of compounds, L.W., X. L., and D.Z.; compound isolation and synthesis, L.G., S.W., and K.T.; molecular docking and DFT calculation, J.P. and J. N.; guidance for writing and experiment and provided strains, M.C., H.J., Y.P., and Y. Yu. All authors have read and agreed to the published version of the manuscript.

DECLARATION OF INTERESTS

The authors declare no competing interests.

STAR★METHODS

Detailed methods are provided in the online version of this paper and include the following:

- KEY RESOURCES TABLE
- EXPERIMENTAL MODEL AND STUDY PARTICIPANT DETAILS
  - Bacterial strains and growth conditions
  - Animals
- METHOD DETAILS
  - Collection of *Streptomyces* genome sequences
  - Phylogenetic tree construction
  - Identification of BGCs
  - Extraction and isolation
  - Structure elucidation
  - UPLC-MS^2 data analysis
  - Cheminformatics analysis
  - Chemical synthesis of 5–9

Figure 7. *In vivo* potency and safety of the combination of bismuth citrate and 7 against ciprofloxacin-resistant *P. aeruginosa*

(A) Scheme of the experimental protocol for establishing the mouse lung infection model.

(B) Therapeutic effect of the combination of bismuth citrate and **7** on *P. aeruginosa* 535 infection in a mouse lung infection model. The bacterial loads (log_{10} CFU [colony-forming unit]) in the lungs were determined (n = 6 animals). Mean ± standard error of the mean (error bars) is shown.

(C) Therapeutic effect of the combination of bismuth citrate and **7** on *P. aeruginosa* 541 infection in a mouse lung infection model. The bacterial loads (log_{10} CFU) in the lungs were determined (n = 6 animals). Mean ± standard error of the mean (error bars) is shown.

(D) H&E staining of mouse lungs at the end of the experiment in the *P. aeruginosa* 541 infection model. Scale bars represent 50 μm.

(E) Survival curves showing the efficacy of the combined treatment in a mouse acute pneumonia model (n = 10 animals). Increased survival rates of mice challenged with a lethal dose of *P. aeruginosa* 541 over 7 days were observed in the mice treated with the combination of bismuth citrate and **7**.

(F) Histopathological examination: H&E staining of the heart, liver, spleen, and kidneys at the end of the experiment in the *P. aeruginosa* 541 infection model. Scale bars represent 50 μm.

(G) The levels of alanine aminotransferase (ALT), aspartate transaminase (AST), blood urea nitrogen (BUN), creatinine (CR), lactate dehydrogenase (LDH), and creatine kinase (CK) were measured in the mouse lung *P. aeruginosa* 541 infection model (n = 6 animals). Blood was collected at the end of the experiment. Mean ± standard error of the mean (error bars) is shown. Cip, ciprofloxacin; BC, bismuth citrate; vehicle, physiological saline.

Statistical comparisons were performed via one-way ANOVA and Dunnett's multiple comparisons test (B, C, E, and G). No significance (ns) $p > 0.05$, $^{**}p < 0.01$, $^{***}p < 0.001$, $^{****}p < 0.0001$.

- Chrome azurol S activity
- Antimicrobial activity test
- Effect of Fe^{3+} on the combined therapy
- Intracellular bismuth ion levels in *P. aeruginosa*
- Resistance assay
- Density functional theory (DFT) calculations
- Membrane depolarization assay
- Membrane integrity assay
- DNA damage assay
- SEM assay
- TEM assay
- ROS detection
- Comet assay
- ATP detection
- Antibiofilm activity of *P. aeruginosa in vitro*
- Proteomic analysis
- Potassium ion assay
- Fluorescence-based evaluation of compound–DNA interaction
- SPR study
- *In vivo* antibacterial activity assessment in lung infection model
- *In vivo* antibacterial activity assessment in a biofilm-associated wound colonization
- Mouse survival rate
- *In vivo* safety evaluation

- QUANTIFICATION AND STATISTICAL ANALYSIS

SUPPLEMENTAL INFORMATION

Supplemental information can be found online at https://doi.org/10.1016/j.xcrm.2026.102637.

Received: July 8, 2025
Revised: November 4, 2025
Accepted: January 27, 2026
Published: February 26, 2026

REFERENCES

1. Brown, E.D., and Wright, G.D. (2016). Antibacterial drug discovery in the resistance era. Nature *529*, 336–343. https://doi.org/10.1038/nature17042.
2. Chen, J., Wang, W., Hu, X., Yue, Y., Lu, X., Wang, C., Wei, B., Zhang, H., and Wang, H. (2024). Medium-sized peptides from microbial sources with potential for antibacterial drug development. Nat. Prod. Rep. *41*, 1235–1263. https://doi.org/10.1039/D4NP00002A.
3. Hsu, J. (2020). How covid-19 is accelerating the threat of antimicrobial resistance. Br. Med. J. *369*, m1983. https://doi.org/10.1136/bmj.m1983.
4. Chen, J., Guo, Y., Wu, Q., Wang, W., Pan, J., Chen, M., Jiang, H., Yin, Q., Zhang, G., Wei, B., et al. (2023). Discovery of new siderophores from a marine *Streptomycetes* sp. via combined metabolomics and analysis of iron-chelating activity. J. Agric. Food Chem. *71*, 6584–6593. https://doi.org/10.1021/acs.jafc.3c00234.
5. He, R., Gu, S., Xu, J., Li, X., Chen, H., Shao, Z., Wang, F., Shao, J., Yin, W.B., Qian, L., et al. (2024). SIDERITE: Unveiling hidden siderophore diversity in the chemical space through digital exploration. iMeta *3*, e192. https://doi.org/10.1101/2023.08.31.555687.
6. Hider, R.C., and Kong, X. (2010). Chemistry and biology of siderophores. Nat. Prod. Rep. *27*, 637–657. https://doi.org/10.1039/B906679A.
7. Ito, A., Nishikawa, T., Matsumoto, S., Yoshizawa, H., Sato, T., Nakamura, R., Tsuji, M., and Yamano, Y. (2016). Siderophore cephalosporin cefiderocol utilizes ferric iron transporter systems for antibacterial activity against *Pseudomonas aeruginosa*. Antimicrob. Agents Chemother. *60*, 7396–7401. https://doi.org/10.1128/aac.01405-16.
8. Karakonstantis, S., Rousaki, M., and Kritsotakis, E.I. (2022). Cefiderocol: Systematic review of mechanisms of resistance, heteroresistance and *in vivo* emergence of resistance. Antibiotics *11*, 723. https://doi.org/10.3390/antibiotics11060723.
9. Streling, A.P., Al Obaidi, M.M., Lainhart, W.D., Zangeneh, T., Khan, A., Dinh, A.Q., Hanson, B., Arias, C.A., and Miller, W.R. (2021). Evolution of cefiderocol non-susceptibility in *Pseudomonas aeruginosa* in a patient without previous exposure to the antibiotic. Clin. Infect. Dis. *73*, e4472–e4474. https://doi.org/10.1093/cid/ciaa1909.
10. Guevara, B., and Cogdill, A.G. (2020). *Helicobacter pylori*: A review of current diagnostic and management strategies. Dig. Dis. Sci. *65*, 1917–1931. https://doi.org/10.1007/s10620-020-06193-7.
11. Westblom, T.U., Madan, E., Subik, M.A., Duriex, D.E., and Midkiff, B.R. (1992). Double-blind randomized trial of bismuth subsalicylate and clindamycin for treatment of *Helicobacter pylori* infection. Scand. J. Gastroenterol. *27*, 249–252. https://doi.org/10.3109/00365529208999958.
12. Olm, M.R., Brown, C.T., Brooks, B., and Banfield, J.F. (2017). dRep: a tool for fast and accurate genomic comparisons that enables improved genome recovery from metagenomes through de-replication. ISME J. *11*, 2864–2868. https://doi.org/10.1038/ismej.2017.126.
13. Parks, D.H., Imelfort, M., Skennerton, C.T., Hugenholtz, P., and Tyson, G.W. (2015). CheckM: assessing the quality of microbial genomes recovered from isolates, single cells, and metagenomes. Genome Res. *25*, 1043–1055. http://www.genome.org/cgi/doi/10.1101/gr.186072.114.
14. Blin, K., Shaw, S., Kloosterman, A.M., Charlop-Powers, Z., van Wezel, G.P., Medema, M.H., and Weber, T. (2021). antiSMASH 6.0: improving cluster detection and comparison capabilities. Nucleic Acids Res. *49*, W29–W35. https://doi.org/10.1093/nar/gkab335.
15. Kautsar, S.A., Blin, K., Shaw, S., Navarro-Muñoz, J.C., Terlouw, B.R., van der Hooft, J.J.J., van Santen, J.A., Tracanna, V., Suarez Duran, H.G., Pascal Andreu, V., et al. (2020). MIBiG 2.0: a repository for biosynthetic gene clusters of known function. Nucleic Acids Res. *48*, D454–D458. https://doi.org/10.1093/nar/gkz882.
16. Navarro-Muñoz, J.C., Selem-Mojica, N., Mullowney, M.W., Kautsar, S.A., Tryon, J.H., Parkinson, E.I., De Los Santos, E.L.C., Yeong, M., Cruz-Morales, P., Abubucker, S., et al. (2020). A computational framework to explore large-scale biosynthetic diversity. Nat. Chem. Biol. *16*, 60–68. https://doi.org/10.1038/s41589-019-0400-9.
17. Katoh, K., and Standley, D.M. (2013). MAFFT multiple sequence alignment software version 7: improvements in performance and usability. Mol. Biol. Evol. *30*, 772–780. https://doi.org/10.1093/molbev/mst010.
18. Nothias, L.F., Petras, D., Schmid, R., Dührkop, K., Rainer, J., Sarvepalli, A., Protsyuk, I., Ernst, M., Tsugawa, H., Fleischauer, M., et al. (2020). Feature-based molecular networking in the GNPS analysis environment. Nat. Methods *17*, 905–908. https://doi.org/10.1038/s41592-020-0933-6.
19. He, Q.F., Wu, Z.L., Li, L., Sun, W.Y., Wang, G.Y., Jiang, R.W., Hu, L.J., Shi, L., He, R.R., Wang, Y., and Ye, W.C. (2021). Discovery of neuritogenic securinega alkaloids from *Flueggea suffruticosa* by a building blocks-based molecular network strategy. Angew. Chem. Int. Ed. *60*, 19609–19613. https://doi.org/10.1002/anie.202103878.
20. Senges, C.H.R., Al-Dilaimi, A., Marchbank, D.H., Wibberg, D., Winkler, A., Haltli, B., Nowrousian, M., Kalinowski, J., Kerr, R.G., and Bandow, J.E. (2018). The secreted metabolome of *Streptomyces chartreusis* and implications for bacterial chemistry. Proc. Natl. Acad. Sci. USA *115*, 2490–2495. https://doi.org/10.1073/pnas.1715713115.
21. Lipinski, C.A., Lombardo, F., Dominy, B.W., and Feeney, P.J. (2001). Experimental and computational approaches to estimate solubility and permeability in drug discovery and development settings. Adv. Drug Deliv. Rev. *46*, 3–26. https://doi.org/10.1016/S0169-409X(00)00129-0.
22. Josts, I., Veith, K., and Tidow, H. (2019). Ternary structure of the outer membrane transporter FoxA with resolved signalling domain provides insights into TonB-mediated siderophore uptake. eLife *8*, e48528. https://doi.org/10.7554/eLife.48528.
23. Normant, V., Josts, I., Kuhn, L., Perraud, Q., Fritsch, S., Hammann, P., Mislin, G.L.A., Tidow, H., and Schalk, I.J. (2020). Nocardamine-dependent

iron uptake in *Pseudomonas aeruginosa*: Exclusive involvement of the FoxA outer membrane transporter. ACS Chem. Biol. *15*, 2741–2751. https://doi.org/10.1021/acschembio.0c00535.

24. Moynié, L., Milenkovic, S., Mislin, G.L.A., Gasser, V., Malloci, G., Baco, E., McCaughan, R.P., Page, M.G.P., Schalk, I.J., Ceccarelli, M., and Naismith, J.H. (2019). The complex of ferric-enterobactin with its transporter from *Pseudomonas aeruginosa* suggests a two-site model. Nat. Commun. *10*, 3673. https://doi.org/10.1038/s41467-019-11508-y.
25. Abraham, M.J., Murtola, T., Schulz, R., Páll, S., Smith, J.C., Hess, B., and Lindahl, E. (2015). GROMACS: High performance molecular simulations through multi-level parallelism from laptops to supercomputers. SoftwareX *1–2*, 19–25. https://doi.org/10.1016/j.softx.2015.06.001.
26. Schrödinger, L., and DeLano, W. (2020). PyMOL (Version 2.0) [Computer software]. http://www.pymol.org/pymol.
27. Neese, F. (2022). Software update: The ORCA program system—Version 5.0. WIREs Comput. Mol. Sci. *12*, e1606. https://doi.org/10.1002/wcms.1606.
28. Lu, T., and Chen, F. (2012). Multiwfn: A multifunctional wavefunction analyzer. J. Comput. Chem. *33*, 580–592. https://doi.org/10.1002/jcc.22885.
29. Lu, T. (2024). A comprehensive electron wavefunction analysis toolbox for chemists, Multiwfn. J. Chem. Phys. *161*, 082503. https://doi.org/10.1063/5.0216272.
30. Guo, Y., Liu, Y., Chen, Y., Du, S., Zheng, Y., and Wang, L. (2025). The mechanisms of environmental pollutant acetyl tributyl citrate induced oral squamous cell carcinoma using network toxicology, molecular docking and molecular dynamics simulation. Int. J. Surg. *111*, 7873–7885. https://doi.org/10.1097/JS9.0000000000002967.
31. Wang, C., Wei, X., Zhong, L., Chan, C.L., Li, H., Sun, H., and Sun, H. (2025). Metal-based approaches for the fight against antimicrobial resistance: Mechanism, opportunities, and challenges. J. Am. Chem. Soc. *147*, 12361–12380. https://doi.org/10.1021/jacs.4c16035.
32. Schalk, I.J. (2025). Bacterial siderophores: diversity, uptake pathways and applications. Nat. Rev. Microbiol. *23*, 24–40. https://doi.org/10.1038/s41579-024-01090-6.
33. Frei, A., Verderosa, A.D., Elliott, A.G., Zuegg, J., and Blaskovich, M.A.T. (2023). Metals to combat antimicrobial resistance. Nat. Rev. Chem *7*, 202–224. https://doi.org/10.1038/s41570-023-00463-4.
34. Wang, H., Wang, M., Xu, X., Gao, P., Xu, Z., Zhang, Q., Li, H., Yan, A., Kao, R.Y.T., and Sun, H. (2021). Multi-target mode of action of silver against *Staphylococcus aureus* endows it with capability to combat antibiotic resistance. Nat. Commun. *12*, 3331. https://doi.org/10.1038/s41467-021-23659-y.
35. Franz, K.J., and Metzler-Nolte, N. (2019). Introduction: metals in medicine. Chem. Rev. *119*, 727–729. https://doi.org/10.1021/acs.chemrev.8b00685.
36. Tsang, C.N., Ho, K.S., Sun, H., and Chan, W.T. (2011). Tracking bismuth antiulcer drug uptake in single *Helicobacter pylori* cells. J. Am. Chem. Soc. *133*, 7355–7357. https://doi.org/10.1021/ja2013278.
37. Bardhan, K.D., Dallaire, C., Eisold, H., and Duggan, A.E. (1997). Ranitidine bismuth citrate with clarithromycin for the treatment of duodenal ulcer. Gut *41*, 181–186. https://doi.org/10.1136/gut.41.2.181.
38. Gaßel, M., and Altendorf, K. (2003). Analysis of KdpC of the K^+-transporting KdpFABC complex of *Escherichia coli*. Eur. J. Biochem. *268*, 1772–1781. https://doi.org/10.1046/j.1432-1327.2001.02048.x.
39. Yu, Y., Jang, M., Miyashiro, J., Clark, R.F., Zhu, G.D., Gong, J., Dai, Y., Frey, R.R., Penning, T.D., Kim, H., et al. (2024). Discovery of A-910, a highly potent and orally bioavailable dual MerTK/Axl-selective tyrosine kinase inhibitor. J. Med. Chem. *67*, 17000–17032. https://doi.org/10.1021/acs.jmedchem.4c01450.
40. Wang, C., Xia, Y., Wang, R., Li, J., Chan, C.L., Kao, R.Y.T., Toy, P.H., Ho, P.L., Li, H., and Sun, H. (2023). Metallo-sideromycin as a dual functional complex for combating antimicrobial resistance. Nat. Commun. *14*, 5311. https://doi.org/10.1038/s41467-023-40828-3.
41. Murdoch, C.C., and Skaar, E.P. (2022). Nutritional immunity: the battle for nutrient metals at the host-pathogen interface. Nat. Rev. Microbiol. *20*, 657–670. https://doi.org/10.1038/s41579-022-00745-6.
42. Xia, Y., Wei, X., Gao, P., Wang, C., de Jong, A., Chen, J.H.K., Rodríguez-Sánchez, M.J., Rodríguez-Nogales, A., Diez-Echave, P., Gálvez, J., et al. (2024). Bismuth-based drugs sensitize *Pseudomonas aeruginosa* to multiple antibiotics by disrupting iron homeostasis. Nat. Microbiol. *9*, 2600–2613. https://doi.org/10.1038/s41564-024-01807-6.
43. Chaumeil, P.A., Mussig, A.J., Hugenholtz, P., and Parks, D.H. (2022). GTDB-Tk v2: memory friendly classification with the genome taxonomy database. Bioinformatics *38*, 5315–5316. https://doi.org/10.1093/bioinformatics/btac672.
44. Nguyen, L.T., Schmidt, H.A., von Haeseler, A., and Minh, B.Q. (2014). IQ-TREE: a fast and effective stochastic algorithm for estimating maximum-likelihood phylogenies. Mol. Biol. Evol. *32*, 268–274. https://doi.org/10.1093/molbev/msu300.
45. Xie, J., Chen, Y., Cai, G., Cai, R., Hu, Z., and Wang, H. (2023). Tree visualization by one table (tvBOT): a web application for visualizing, modifying and annotating phylogenetic trees. Nucleic Acids Res. *51*, 587–592. https://doi.org/10.1093/nar/gkad359.
46. Su, G., Morris, J.H., Demchak, B., and Bader, G.D. (2014). Biological network exploration with Cytoscape 3. Curr. Protoc. Bioinf. *47*, 8.13.1–8.13.24. https://doi.org/10.1002/0471250953.bi0813s47.
47. Liu, Y., Yang, X., Gan, J., Chen, S., Xiao, Z.X., and Cao, Y. (2022). CB-Dock2: improved protein–ligand blind docking by integrating cavity detection, docking and homologous template fitting. Nucleic Acids Res. *50*, 159–164. https://doi.org/10.1093/nar/gkac394.
48. Yang, X., Liu, Y., Gan, J., Xiao, Z.X., and Cao, Y. (2022). FitDock: protein–ligand docking by template fitting. Brief. Bioinform. *23*, bbac087. https://doi.org/10.1093/bib/bbac087.
49. Parks, D.H., Chuvochina, M., Chaumeil, P.A., Rinke, C., Mussig, A.J., and Hugenholtz, P. (2020). A complete domain-to-species taxonomy for bacteria and archaea. Nat. Biotechnol. *38*, 1079–1086. https://doi.org/10.1038/s41587-020-0501-8.
50. Matsen, F.A., Kodner, R.B., and Armbrust, E.V. (2010). pplacer: linear time maximum-likelihood and bayesian phylogenetic placement of sequences onto a fixed reference tree. BMC Bioinf. *11*, 538. https://doi.org/10.1186/1471-2105-11-538.
51. Jain, C., Rodriguez-R, L.M., Phillippy, A.M., Konstantinidis, K.T., and Aluru, S. (2018). High throughput ANI analysis of 90K prokaryotic genomes reveals clear species boundaries. Nat. Commun. *9*, 5114. https://doi.org/10.1038/s41467-018-07641-9.
52. Hyatt, D., Chen, G.L., Locascio, P.F., Land, M.L., Larimer, F.W., and Hauser, L.J. (2010). Prodigal: prokaryotic gene recognition and translation initiation site identification. BMC Bioinf. *11*, 119. https://doi.org/10.1186/1471-2105-11-119.
53. Eddy, S.R. (2011). Accelerated profile HMM searches. PLoS Comput. Biol. *7*, e1002195. https://doi.org/10.1371/journal.pcbi.1002195.
54. Ondov, B.D., Treangen, T.J., Melsted, P., Mallonee, A.B., Bergman, N.H., Koren, S., and Phillippy, A.M. (2016). Mash: fast genome and metagenome distance estimation using MinHash. Genome Biol. *17*, 132. https://doi.org/10.1186/s13059-016-0997-x.
55. Hoang, D.T., Chernomor, O., von Haeseler, A., Minh, B.Q., and Vinh, L.S. (2018). UFBoot2: improving the ultrafast bootstrap approximation. Mol. Biol. Evol. *35*, 518–522. https://doi.org/10.1093/molbev/msx281.
56. Kalyaanamoorthy, S., Minh, B.Q., Wong, T.K.F., von Haeseler, A., and Jermiin, L.S. (2017). ModelFinder: fast model selection for accurate phylogenetic estimates. Nat. Methods *14*, 587–589. https://doi.org/10.1038/nmeth.4285.
57. Edgar, R.C. (2022). Muscle5: High-accuracy alignment ensembles enable unbiased assessments of sequence homology and phylogeny. Nat. Commun. *13*, 6968. https://doi.org/10.1038/s41467-022-34630-w.

58. Chambers, M.C., MacLean, B., Burke, R., Amodei, D., Ruderman, D.L., Neumann, S., Gatto, L., Fischer, B., Pratt, B., Egertson, J., et al. (2012). A cross-platform toolkit for mass spectrometry and proteomics. Nat. Biotechnol. *30*, 918–920. https://doi.org/10.1038/nbt.2377.

59. Pluskal, T., Castillo, S., Villar-Briones, A., and Oresic, M. (2010). MZmine 2: modular framework for processing, visualizing, and analyzing mass spectrometry-based molecular profile data. BMC Bioinf. *11*, 395. https://doi.org/10.1186/1471-2105-11-395.

60. Wang, M., Carver, J.J., Phelan, V.V., Sanchez, L.M., Garg, N., Peng, Y., Nguyen, D.D., Watrous, J., Kapono, C.A., Luzzatto-Knaan, T., et al. (2016). Sharing and community curation of mass spectrometry data with Global Natural Products Social Molecular Networking. Nat. Biotechnol. *34*, 828–837. https://doi.org/10.1038/nbt.3597.

61. Wang, Z., Koirala, B., Hernandez, Y., Zimmerman, M., and Brady, S.F. (2022). Bioinformatic prospecting and synthesis of a bifunctional lipopeptide antibiotic that evades resistance. Science *376*, 991–996. https://doi.org/10.1126/science.abn4213.

62. Ma, Y., Guo, Z., Xia, B., Zhang, Y., Liu, X., Yu, Y., Tang, N., Tong, X., Wang, M., Ye, X., et al. (2022). Identification of antimicrobial peptides from the human gut microbiome using deep learning. Nat. Biotechnol. *40*, 921–931. https://doi.org/10.1038/s41587-022-01226-0.

63. Song, M., Liu, Y., Huang, X., Ding, S., Wang, Y., Shen, J., and Zhu, K. (2020). A broad-spectrum antibiotic adjuvant reverses multidrug-resistant Gram-negative pathogens. Nat. Microbiol. *5*, 1040–1050. https://doi.org/10.1038/s41564-020-0723-z.

64. Hua, S., Hu, H., Liu, J., Lu, F., Yu, R., Zhang, X., Sun, H., Wang, Z., Li, Y., Xia, J., et al. (2024). A mucous permeable local delivery strategy based on manganese-enhanced bacterial cuproptosis-like death for bacterial pneumonia treatment. ACS Nano *18*, 31923–31940. https://doi.org/10.1021/acsnano.4c09695.

65. Niu, L., Zhang, H., Wu, Z., Wang, Y., Liu, H., Wu, X., and Wang, W. (2018). Modified TCA/acetone precipitation of plant proteins for proteomic analysis. PLoS One *13*, e0202238. https://doi.org/10.1371/journal.pone.0202238.

66. Zhang, H., Liu, T., Zhang, Z., Payne, S.H., Zhang, B., McDermott, J.E., Zhou, J.Y., Petyuk, V.A., Chen, L., Ray, D., et al. (2016). Integrated proteogenomic characterization of human high-grade serous ovarian cancer. Cell *166*, 755–765. https://doi.org/10.1016/j.cell.2016.05.069.

67. Huang, D.W., Sherman, B.T., and Lempicki, R.A. (2009). Bioinformatics enrichment tools: paths toward the comprehensive functional analysis of large gene lists. Nucleic Acids Res. *37*, 1–13. https://doi.org/10.1093/nar/gkn923.

68. Franceschini, A., Szklarczyk, D., Frankild, S., Kuhn, M., Simonovic, M., Roth, A., Lin, J., Minguez, P., Bork, P., von Mering, C., and Jensen, L.J. (2013). STRING V9.1: Protein-protein interaction networks, with increased coverage and integration. Nucleic Acids Res. *41*, D808–D815. https://doi.org/10.1093/nar/gks1094.

STAR★METHODS

KEY RESOURCES TABLE

REAGENT or RESOURCE	SOURCE	IDENTIFIER
Chemicals, peptides, and recombinant proteins		
1–9	This paper	N/A
Bismuth citrate	Adamas-beta	Cat#ADB84628002; CAS:813-93-4
Ciprofloxacin	Sigma-Aldrich	Cat#PHR1167; CAS:85721-33-1
Levofloxacin	Perfemiker	Cat#C84-5098; CAS:177325-13-2
Norfloxacin	Adamas-beta	Cat#AL78150001; CAS:70458-96-7
4′,6-Diamidino-2-Phenylindole solution	Beyotime	Cat#C1002
3,3′-dipropylthiadicarbocyanine iodide	Sigma-Aldrich	Cat#43608; CAS:53213-94-8
Propidium iodide	Sigma-Aldrich	Cat#79214; CAS:25535-16-4
Dimethyl sulfoxide (DMSO)	Sigma-Aldrich	Cat#D8418; CAS:67-68-5
LB broth	Hopebiol	Cat#HB0128
Cyclophosphamide	Bidepharm	Cat#BD122996; CAS:50-18-0
Critical commercial assays		
Bacterial oxidative stress reactive oxygen fluorescence assay kit	JIWEI	Cat#G&VS10016.14
Bacterial DNA damage comet assay kit	GENMED	Cat#GMS10082.1
Micro ATP content detection kit	Abbkine	Cat#KTB1016
BCA kit	Beyotime	Cat#P0010S
TIANamp bacteria DNA kiit	TIANGEN	Cat#DP302
Deposited data		
Proteomics	This paper	PRIDE (PRoteomics IDEntifications Database): PXD069942; PXD070105
Raw images	This paper	N/A
Metabolomics Data	This paper	N/A
Immunohistochemical staining - H&E staining	This paper	N/A
Molecular docking	This paper	N/A
Molecular dynamics simulation	This paper	N/A
Mouse gastrointestinal genome	This paper	NCBI: SUB15712967
Experimental models: Organisms/strains		
ICR (SPF) mouse	Hangzhou Qizhen Experimental Animal Technology Co., Ltd	N/A
BALB/c mouse	Hangzhou Qizhen Experimental Animal Technology Co., Ltd	N/A
P. aeruginosa 541	The Second Affiliated Hospital, Zhejiang University School of Medicine, China	N/A
P. aeruginosa 535	The Second Affiliated Hospital, Zhejiang University School of Medicine, China	N/A
P. aeruginosa 9337	The Second Affiliated Hospital, Zhejiang University School of Medicine, China	N/A
P. aeruginosa 859	The Second Affiliated Hospital, Zhejiang University School of Medicine, China	N/A
P. aeruginosa 6302	The Second Affiliated Hospital, Zhejiang University School of Medicine, China	N/A
P. aeruginosa 7034	The Second Affiliated Hospital, Zhejiang University School of Medicine, China	N/A

(*Continued on next page*)

Continued

REAGENT or RESOURCE	SOURCE	IDENTIFIER
P. aeruginosa 9241	The Second Affiliated Hospital, Zhejiang University School of Medicine, China	N/A
P. aeruginosa BHKS396	Heilongjiang Academy of Sciences, China	N/A
S. fradiae FIMYZ-003	Fujian Institute of Microbiology, China	N/A
Software and algorithms		
CheckM	Parks et al.[13]	Version 1.2.2
GTDB-TK	Chaumeil et al.[43]	Version 2.3.2
IQTREE	Nguyen et al.[44]	Version 2.2.2.7
AntiSMASH	Blin et al.[14]	Version 6 local
Wlabkit	–	https://github.com/BioGavin/wlabkit
MAFFT	Katoh et al.[17]	Version 7.520
Chiplot	Xie et al.[45]	https://www.chiplot.online
BiG-SCAPE	Navarro et al.[18]	https://github.com/medema-group/BiG-SCAPE
Cytoscape	Su et al.[46]	Version 3.10.1
GNPS-FBMN	Nothias et al.[18]	https://gnps.ucsd.edu
PyMOL	Schrödinger	Version 3.1.0
AutoDock	The Scripps Research Institute	Version 4.2
Rdkit	RDKit: Open-source cheminformatics.	https://github.com/rdkit/rdkit
Materials studio	Accelrys	Version 2019
ImageJ	National Institutes of Health	https://imagej.net/ij/download.html.
dRep	Olm et al.[12]	Version 3.4.5
CB-Dock2	Liu et al.[47]; Yang et al.[48]	https://cadd.labshare.cn/cb-dock2/php/index.php
GROMACS	Abraham et al.[25]	Version 2021.7
ORCA program	Neese et al.[27]	Version 5.0
Multiwfn	Lu et al.[28,29]	Version 2.1.2
CASP	Comet Assay Software Project Lab	Version 1.2.3 beat 1
SCIEX OS Software	SCIEX	Version 2021
Python script to extract detailed information generated by antiSMASH	This paper	https://doi.org/10.5281/zenodo.18213340

EXPERIMENTAL MODEL AND STUDY PARTICIPANT DETAILS

Bacterial strains and growth conditions

S. fradiae FIMYZ-003 was used for the isolation and purification of siderophores. *P. aeruginosa* strains 541, 535, 6302, 9337, 859, 7034, 9241 and BHKS396 were used for antipseudomonal assays. *S. fradiae* FIMYZ-003 was cultured in liquid medium (15 g/L soluble starch, 5 g/L tryptone, 0.66 g/L $K_2HPO_4{\cdot}3H_2O$, 5 g/L yeast extract, 0.25 g/L $MgSO_4$, 5 g/L glucose, 1 g/L $CaCO_3$, 0.5 g/L $(NH_4)_2SO_4$, 0.5 g/L NaCl; pH 7.0) at 180 rpm and 28°C. *P. aeruginosa* was grown in Luria-Bertani (LB) broth or on LB agar plates at 37°C in an incubator.

Animals

Specific-pathogen-free (SPF) ICR mice (male and female, 4–6 weeks old) and BALB/c mice (female, 4–6 weeks old) were obtained from Hangzhou Qizhen Experimental Animal Technology Co., Ltd. All the mice were housed on an *ad libitum* diet in the SPF facility under the following conditions: dark/light cycle of 12 h, ambient temperature of 22°C–25°C, and humidity of 40–60%. All animal experimental procedures were conducted in accordance with the guidelines of the Institutional Animal Care and Use Committee (IACUC) of Zhejiang University of Technology. The experiments were performed in accordance with the relevant ethical guidelines and regulations. For experiments involving BALB/c mice, only female mice were used to maintain consistency with established protocols in the literature regarding this specific experimental model; therefore, the influence of sex on the results was not evaluated for this specific model.

METHOD DETAILS

Collection of *Streptomyces* genome sequences

A total of 3,013 *Streptomyces* genome sequences were retrieved from the NCBI database. The accession numbers of the dataset are listed in Data S1. The genomes were dereplicated by using dRep v3.4.5 with the criterion set at average nucleotide identity (ANI) of ≥99%. The genome sequences were evaluated using CheckM v1.2.2,[13] and those with contamination <5% and completeness >95% were retained for further analysis. The genome sequences used for further investigations are also listed in Supporting Information Data S1. Ultimately, a total of 1,641 genome sequences with high assembly quality were included to evaluate the encoded secondary metabolites.

Phylogenetic tree construction

All the genome sequences were aligned via GTDB-TK v2.3.2,[43,49–54] using the command "gtdbtk classify_wf". The maximum-likelihood phylogenetic tree was constructed by IQ-TREE v2.2.2.7, using the Modelfinder Plus (MFP) model with 1,000 bootstraps and the "bnni" parameter to optimize UFBoot trees by the nearest neighbor interchange (NNI) algorithm on bootstrap alignment.[44,55,56] The phylogenetic trees of the gene clusters were constructed as follows. The BGCs were predicted by antiSMASH 6.0. We used the Wlabkit tool (https://github.com/BioGavin/wlabkit) to convert all the gbk files to fasta files and concatenated all the fasta files into one fasta file. Then, we aligned the protein sequences by using MAFFT v7.520.[57] The maximum-likelihood phylogenetic tree was constructed by IQ-TREE v2.2.2.7, with the same parameters as above. The phylogenetic trees were visualized and edited with ChiPlot, an online tool.[45]

Identification of BGCs

BGCs encoding the synthesis of natural products were predicted and annotated using the command-line version of antiSMASH 6.1.1.[14] By using a Python script, corresponding information on each class of BGCs was extracted from the HTML files. To evaluate the diversity and novelty, all the siderophore BGCs were extracted from the antiSMASH output files and submitted to BiG-SCAPE for comparison with known BGCs in the MIBiG database using the default parameters. Cytoscape 3.10.1 was used to visualize the similarity network,[46] with each node representing a BGC and similar BGCs being connected by edges. The color of each node represents its similarity to BGCs involved in the biosynthesis of known siderophores. The values of similarity were obtained from HTML files generated by antiSMASH.

Extraction and isolation

FIMYZ-003 was cultured in liquid medium (15 g/L soluble starch, 5 g/L tryptone, 0.66 g/L $K_2HPO_4{\cdot}3H_2O$, 5 g/L yeast extract, 0.25 g/L $MgSO_4$, 5 g/L glucose, 1 g/L $CaCO_3$, 0.5 g/L $(NH_4)_2SO_4$, 0.5 g/L NaCl; pH 7.0; total volume 30 L) for 7 days at 180 rpm and 28°C and then centrifuged for 20 min to remove mycelia. The supernatant was concentrated to 2 L, and the crude extract was obtained by extraction with ethyl acetate (EtOAc). FIMYZ-003 was fermented in the solid state by culturing quiescently at 28°C for 30 days (5 g/L yeast extract, 1 g/L $CaCO_3$, 5 g/L glucose, 5 g/L tryptone, 15 g/L soluble starch, 0.5 g/L $(NH_4)_2SO_4$, 0.5 g/L NaCl, 0.66 g/L $K_2HPO_4{\cdot}3H_2O$, 0.25 g/L $MgSO_4$, 10 g/L agar, pH 7.0). The culture supernatants were extracted twice with an equal volume of EtOAc. The resulting organic phase was then concentrated *in vacuo*, giving rise to the crude extracts.

The crude extracts were separated by an MCI GEL (CHP20/P30) with gradient elution. The elution conditions for the liquid-state extract were as follows: H_2O/MeOH (from 90:10, 70:30, 50:50, 30:70, 10:90 to 0:100) and acetone, using 1 L of solution for each gradient at a flow rate of 30 mL/min, designated G2–G8. The elution conditions for the solid-state extract were as follows: H2O/MeOH (from 90:10, 70:30, 50:50, 30:70 to 0:100) and acetone, using of 1 L of solution for each gradient at a rate of 30 mL/min, designated Y1–Y6.

Crude extract samples G2–G8 and Y1–Y6 were fractionated via semipreparative high-performance liquid chromatography (HPLC) (Xbridge BEH C18 OBD, 5 μm 130 Å, 250 × 10 mm, Waters, USA) with gradient elution at 3 mL/min. A gradient of MeOH/H_2O from 10:90 to 100:0 was used for 30 min. Based on UPLC-MS^2 analysis, fraberin (**1**, 2 mg) was separated.

Structure elucidation

Fraberin (**1**): The product was a yellow powder. The NMR data are shown in Figures S3A–S3F and Table S1. UV(MeOH) λmax (log ε) 194 (0.47) nm (Figure S3G). IR (KBr) νmax cm^{-1}: 3320.14, 2972.54, 2880.74, 1087.63, 1046.15, 879.96 (Figure S3H); HRESI-MS m/z 203.1361 $[M + H]^+$, calcd 203.1396 (Figure S3I).

UPLC-MS^2 data analysis

UPLC-MS2 data were acquired via ultra-performance liquid chromatography (Shimadzu, Kyoto, Japan) together with X500B quantitative time-of-flight (QTOF) mass spectrometry (AB SCIEX, Foster City, CA, USA). The extract samples G2–G8 and Y1–Y6 were analyzed by UPLC-MS^2 using a Poroshell 120 SB−18 column at 35°C, with a gradient elution of MeOH/H_2O from 10:90 to 100:0 at 0.3 mL/min for 30 min, followed by an isocratic elution of MeOH/H_2O 100:0 at 0.3 mL/min for 5 min. The ion spray voltage was 5,500 V, and in positive mode, the ionization source was electrospray ionization (ESI). The full scan range was *m/z* 100 to 2,000

Da, and the fragment ion scan range was *m/z* 50 to 1,000 Da. Information-dependent acquisition (IDA) data were obtained by dynamic background subtraction. SCIEX OS analysis software (version 2.1.6) was used for data acquisition and analysis.

UPLC-MS^2 data were converted into mzXML format with MSConvert (version 3.0.22105 32 bit).[58] MZmine 2.53 was used to process the mzXML files as follows[59]: (1) MS1 noise level; mass detection = retention time (RT), auto, 1.0 E3; MS2 noise level, 2.0 E1. (2) ADAP chromatogram builder = RT, auto; MS-level, 1; minimum group size in no. of scans, 5; *m/z* tolerance (MT), 0.0 *m/z* or 20 ppm; group intensity threshold, 5.0 E2; and minimum highest intensity, 1.0 E3. (3) Deconvolution of UPLC-MS2 chromatograms = baseline-cutoff algorithm; peak duration, 0.1–2 min; minimum peak height, 1.0 E3; and baseline level, 2.5 E2. (4) Isotopic peak grouper = MT, 0.0 *m/z* or 20 ppm; 0.2 min, maximum charge; RT tolerance, 3. (5) Join aligner = MT, 0.1 min, 20 ppm or 0.0 *m/z*, RT tolerance. The final resulting feature list was exported to the mgf and csv formats together using the "Export for GNPS-FBMN" options.

Using the feature-based molecular network workflow (version 1.3.16) on Global Natural Products Social Molecular Networking (GNPS),[60] a molecular network was created by inputting the mgf file and the csv file. The cosine score was set at 0.7 to filter out irrelevant signals.

Cheminformatics analysis

The molecular weight (MW), lipid–water partition coefficient (logP), and quantitative estimates of drug-likeness (QED), H-bond donor (HBD) ability and H-bond acceptor (HBA) ability were calculated by RDKit.

The TonB-dependent receptor FemA (PDB: 9F2T), FoxA (PDB: 6Z8A), FptA (PDB: 1XKW), FpvA (PDB: 2W6T), OprC (PDB: 6Z8S), PfeA (PDB: 5NC3), PhuR (PDB: 8THE), PirA (PDB: 5FP2), PiuA (PDB: 5FOK), and Pa5505 (PDB: 4K3F; a putative TonB-dependent receptor) were downloaded from the RCSB PDB (Protein DataBank), and FiuA and FpvB were downloaded from UniProt. Cavity was searching based on a protein surface curvature-based cavity detection approach on CB-Dock2.[47,48] The iron-chelated siderophores (**1**–Fe^{3+}, ferrioxamine B–Fe^{3+}, nocardamine–Fe^{3+}, and enterobactin–Fe^{3+}) were uploaded and served as ligands. Docking was then conducted using CB-Dock2, an AutoDock-Vina based online docking tool, to characterize their binding modes. Docking results were analyzed and visualized using PyMOL.

MD simulations were conducted by using GROMACS with the amber99sb force field. The MD system was prepared by solvation with TIP3P water and neutralization with ions. After energy minimization and equilibration in NVT and NPT ensembles, a 300-ns production simulation was carried out. The simulation employed a 2-fs integration time step under constant temperature (310 K) and pressure (1.0 bar). Long-range electrostatics were handled with the PME method. Periodic boundary conditions were applied in all three directions throughout the simulation. Data analysis was performed by using GROMACS to calculate the RMSD, RMSF, Rg, and system free energy, as well as to construct the free energy landscape. Molecular visualization was conducted by using PyMOL.

AutoDock4 was employed to characterize the binding modes of compound **7**, its bismuth complex (**7**–Bi), and bismuth citrate with DNA (PDB: 7XAQ). The DNA structure was preprocessed in AutoDockTools (ADT) by removing crystallographic water, adding hydrogens, and assigning Gasteiger-Marsili charges. Ligands were converted to PDBQT format after atom type and charge assignment. A global docking box encompassing the entire DNA was defined using the Grid module, and affinity grids (van der Waals, electrostatic, hydrogen bonds) were generated using AutoGrid. The Lamarckian GA (LGA) algorithm was used for docking, with output conformations selected based on lowest AMBER-predicted binding energy. Interactions were analyzed using PLIP and visualized in PyMOL.

Chemical synthesis of 5–9

Compound **I** was synthesized via *t*-butyloxy carbonyl (Boc) protection of ciprofloxacin. The reduction of *O*-benzylhydroxylamine hydrochloride by acyl chloride, followed by the substitution of the imine functional group with an *N*-Boc-3-aminopropyl bromide analog, led to the formation of the ferredoxin analog **II**. The ciprofloxacin–fraberin conjugates (**5**–**9**) were synthesized via an amide coupling reaction between **I** and the ferredoxin analog **II** (Figure S6A).

5: ^{1}H NMR (500 MHz, DMSO-d_6) δ 15.13 (s, 1H), 9.73 (s, 1H), 8.63 (s, 1H), 7.86 (d, *J* = 13.1 Hz, 1H), 7.79 (t, *J* = 5.8 Hz, 1H), 7.56 (m, 1H), 3.81 (s, 1H), 3.68 (d, *J* = 20.9 Hz, 4H), 3.49 (t, *J* = 7.1 Hz, 2H), 3.29 (s, 2H), 3.02 (q, *J* = 6.5 Hz, 2H), 2.60–2.56 (m, 4H), 1.78 (s, 3H), 1.64 (h, *J* = 6.4 Hz, 2H), 1.33 (d, *J* = 6.7 Hz, 2H), 1.18 (s, 2H). ^{13}C NMR (125 MHz, DMSO-d_6) δ 176.31, 172.15, 170.21, 169.05, 165.87, 151.92, 147.97, 144.96, 139.11, 118.76, 111.05, 106.75, 106.51, 49.56, 49.2, 45.51, 44.43, 36.30, 35.87, 27.19, 26.85, 26.71, 22.61, 7.59. HRESI-MS, $C_{26}H_{32}FN_5O_7$, *m/z* 546.2348 $[M + H]^+$, calcd 546.2359 (Figures S6B–S6D).

6: ^{1}H NMR (500 MHz, DMSO-d_6) δ 14.99 (s, 1H), 9.79 (m, 1H), 8.63 (s, 1H), 7.88 (d, *J* = 13.3 Hz, 2H), 7.55 (s, 1H), 3.74 (d, *J* = 23.3 Hz, 5H), 3.49 (t, *J* = 7.3 Hz, 2H), 3.29 (d, *J* = 21.7 Hz, 4H), 3.02 (q, *J* = 6.6 Hz, 2H), 2.52 (s, 4H), 1.77 (s, 3H), 1.63 (t, *J* = 7.3 Hz, 2H), 1.32 (s, 2H), 1.17 (s, 2H), 1.08 (s, 6H). ^{13}C NMR (125 MHz, DMSO-d_6) δ 176.24, 171.54, 169.73, 169.02, 165.94, 151.90, 147.94, 144.86, 139.07, 118.89, 111.05, 107.13, 106.54, 49.63, 49.34, 45.31, 45.20, 41.38, 41.19, 40.48, 36.34, 35.82, 33.17, 27.88, 26.75, 22.60, 7.58. HRESI-MS, $C_{29}H_{38}FN_5O_7$, *m/z* 588.2819 $[M + H]^+$, calcd 588.2828 (Figures S7A–S7C).

7: ^{1}H NMR (500 MHz, DMSO-d_6) δ 15.15 (s, 1H), 9.68 (s, 1H), 8.63 (s, 1H), 7.85 (d, *J* = 13.1 Hz, 2H), 7.56 (s, 1H), 3.70 (d, *J* = 57.2Hz, 5H), 3.46 (s, 2H), 3.29 (s, 2H), 3.02 (s, 2H), 2.61 (t, *J* = 7.0 Hz, 2H), 2.35 (s, 2H), 1.97 (s, 3H), 1.50 (s, 2H), 1.40 (d, *J* = 29.4 Hz, 4H), 1.19 (d, *J* = 25.1 Hz, 4H). ^{13}C NMR (125 MHz, DMSO-d_6) δ 176.28, 171.13, 170.13, 165.85, 151.90, 147.94, 144.94, 139.09, 118.74, 111.04, 106.74, 106.46, 49.56, 49.21, 46.79, 44.42, 40.75, 38.43, 35.85, 30.37, 28.83, 27.82, 26.04, 23.50, 20.34, 7.58. HRESI-MS, $C_{28}H_{36}FN_5O_7$, *m/z* 574.2657 $[M + H]^+$, calcd 574.2672 (Figures S7D–S7F).

8: ^{1}H NMR (500 MHz, DMSO-d_6) δ 15.17 (s, 1H), 9.72 (s, 1H), 8.64 (s, 1H), 7.90 (m, 2H), 7.57 (d, *J* = 7.3 Hz, 1H), 3.81 (tt, *J* = 7.4, 4.1 Hz, 1H), 3.72 (dt, *J* = 19.3, 5.3 Hz, 4H), 3.53 (t, *J* = 6.7 Hz, 2H), 3.37 (dt, *J* = 6.3, 2.8 Hz, 2H), 3.29 (d, *J* = 5.3 Hz, 2H), 3.21 (q, *J* = 6.6 Hz, 2H), 2.65-2.50 (m, 4H), 1.79 (s, 3H), 1.33 (dd, *J* = 7.5, 5.6 Hz, 2H), 1.19 (m, 2H). ^{13}C NMR (125 MHz, DMSO-d_6) δ 176.33, 172.55, 170.18, 169.93, 165.88, 151.93, 148.00, 144.96, 139.12, 118.78, 111.07, 106.75, 106.55, 49.55, 49.20, 46.85, 44.42, 40.79, 35.87, 35.72, 27.14, 26.88, 22.55, 7.59. HRESI-MS, $C_{25}H_{30}FN_5O_7$, *m/z* 532.2200 $[M + H]^+$, calcd 532.2202 (Figures S8A–S8C).

9: ^{1}H NMR (500 MHz, DMSO-d_6) δ 15.16 (s, 1H), 9.65 (s, 1H), 8.64 (s, 1H), 7.91 (d, *J* = 13.1 Hz, 1H), 7.80 (t, *J* = 5.6 Hz, 1H), 7.57 (d, *J* = 7.3 Hz, 1H), 3.81 (s, 1H), 3.68 (p, *J* = 4.8 Hz, 4H), 3.45 (t, *J* = 7.1 Hz, 2H), 3.34 (m, 2H), 3.29 (t, *J* = 5.1 Hz, 2H), 3.01 (q, *J* = 6.5 Hz, 2H), 2.59 (t, *J* = 7.0 Hz, 2H), 2.33 (t, *J* = 7.0 Hz, 2H), 1.95 (s, 3H), 1.49 (p, *J* = 7.1 Hz, 2H), 1.36 (m, 4H), 1.21 (m, 6H). ^{13}C NMR (125 MHz, DMSO-d_6) δ 176.32, 173.92, 171.08, 170.12, 165.88, 151.93, 148.01, 144.88, 139.12, 118.79, 111.08, 106.75, 106.54, 49.56, 49.21, 46.84, 44.42, 40.75, 38.42, 35.87, 30.36, 29.09, 27.81, 26.28, 26.08, 25.83, 20.33, 7.59. HRESI-MS, $C_{29}H_{38}FN_5O_7$, *m/z* 588.2832 $[M + H]^+$, calcd 588.2828 (Figures S8D–S8F).

Chrome azurol S activity

Chrome azurol S (CAS) (60.5 mg) was weighed and dissolved in 50.0 mL deionized water, followed by the slow addition of 10.0 mL of 1 mM $FeCl_3$ in 10 mM HCl solution under magnetic stirring to obtain Solution A. Separately, cetyltrimethylammonium bromide (CTAB) (72.9 mg) was weighed and dissolved in 40.0 mL deionized water to obtain Solution B. Solutions A and B were mixed and vortexed for 1 min to ensure thorough mixing, yielding the CAS assay solution, which was stored at 4°C.

For siderophore detection, a 1 mg/mL solution of the test sample was prepared in methanol, and 50 μL was transferred to a well of a 96-well plate. Then, 50 μL of CAS assay solution was added, and the mixture was incubated at 25°C protected from light for 10–15 min. The color change was observed under white light, with 50 μL of 1 mg/mL deferoxamine mesylate (DFOB) methanol solution used as the positive control and an equal volume of methanol used as the negative control. The appearance of an orange-red to purple-red color indicated the presence of siderophore activity.

Antimicrobial activity test

The standard microdilution method was used to determine the MIC according to the Clinical and Laboratory Standards Institute guidelines. All experiments were performed with three independent replicates. A microdilution checkerboard was used for combination drug testing against *P. aeruginosa*. Briefly, the compound or bismuth citrate was added, followed by 2-fold serial dilution with the bacterial suspension. Both the compound and bismuth citrate were diluted 2-fold sequentially in a two-dimensional manner. The interactions between the compounds and bismuth citrate were determined as follows: synergistic (FICI $\leq$0.5), additive (0.5<FICI$\leq$1), no interaction (1<FICI$\leq$2), or antagonistic (FICI >2). The FICI was calculated by using the following equation:

$$FICI = Ccompound, combination / Ccompound, alone + Cbismuth\ citrate, combination / Cbismuth\ citrate.$$

Effect of Fe^{3+} on the combined therapy

An overnight culture of *P. aeruginosa* 9337 was centrifuged (10,000 rpm, 5 min, 4°C), and the pellet was washed twice with sterile water and subsequently resuspended 1:10,000 in LB medium supplemented with varying concentrations of $FeCl_3{\cdot}6H_2O$ (0 μM, 50 μM, 100 μM, and 500 μM). The impact of iron availability on the combined bactericidal efficacy of **7** and bismuth citrate was evaluated by a checkerboard microdilution assay. Bacterial growth was quantified by measuring the optical density at 600 nm (OD_{600}) on a microplate reader. The FICI was calculated as follows:

$$FICI = Ccompound\ \mathbf{7}, combination / Ccompound\ \mathbf{7}, alone + Cbismuth\ citrate, combination / Cbismuth\ citrate.$$

Intracellular bismuth ion levels in *P. aeruginosa*

P. aeruginosa 541 was cultured overnight, and the bacterial cells were harvested by centrifugation. The pellet was washed, resuspended in physiological saline, and equally divided into two experimental groups. These groups were treated with 128 μg/mL bismuth citrate alone or with 16 μg/mL compound **7** in combination with 128 μg/mL bismuth citrate, respectively. Samples were collected at designated time points (0.5 h, 1 h, 2 h, and 6 h) and centrifuged at 10,000 rpm for 5 min at 4°C.

The microwave digestion procedure was as follows. A 1.0-mL aliquot of the centrifuged bacterial broth was accurately measured and transferred into a microwave digestion vessel, followed by the addition of 6 mL of nitric acid and 3 mL of hydrochloric acid, and the mixture was gently swirled to ensure thorough contact between the sample and the acids. After the reaction stabilized, the vessel was sealed tightly. The loaded digestion vessel was then placed into the microwave digestion system, and digestion was performed with the following program (1) increase to 120°C and holding for 6 min; and (2) a further increase to 180°C and hold for 20 min. The program was initiated to carry out the digestion. Upon completion, the vessel was allowed to cool to room temperature and then carefully vented. It was subsequently placed on an acid evaporation apparatus set at 160°C, in which the solution was heated until nearly dry. After cooling slightly, the inner walls of the vessel were repeatedly rinsed with a small amount of a 1% nitric acid solution, and the dissolved contents were completely transferred into a 10-mL volumetric flask. Finally, the solution was diluted to the mark with 1% nitric acid, thoroughly mixed, and made ready for analysis. Quantification of bismuth in the samples was performed by

ICP-MS. A standard curve was constructed by using bismuth citrate, and the bismuth concentrations in the samples were calculated based on the corresponding signal responses.

Percentage (%) = ($C_{\text{bismuth citrate}}$ -$C_{\text{combination}}$)/$C_{\text{bismuth citrate}}$ × 100%, where $C_{\text{bismuth citrate}}$ is the extracellular bismuth ion concentration following bismuth citrate monotherapy, and $C_{\text{combination}}$ is the extracellular bismuth ion following treatment with the combination of compound **7** and bismuth citrate.

The data at identical time points are shown.

Resistance assay

An *in vitro* evaluation of the potential for *P. aeruginosa* 859 and *P. aeruginosa* 7034 cells to develop resistance to the combination of bismuth citrate and compound **7** was performed as follows. On day 1, overnight cultures grown from single colonies of *P. aeruginosa* 859 and *P. aeruginosa* 7034 in LB at 37°C with shaking at 180 rpm were subjected to microbroth dilution-based susceptibility testing performed using a standard doubling dilution as described for MIC determination. Cultures from the highest concentration that supported growth were diluted 1:10000 in LB medium and used to provide the inoculum for the next passage day. This process was performed for a total duration of 20 days. Aztreonam was used as a positive control.

Density functional theory (DFT) calculations

The B3LYP method was adopted in conjunction with the DND4.4 basis set, and the computations were carried out via the Dmol3 program package within Materials Studio software. To guarantee the accuracy and reliability of the results, computational parameters, including convergence criteria and simulation steps, were meticulously optimized. We successfully obtained stable configurations of compound **7** bound to Bi^{3+} and Fe^{3+}. Further calculations were conducted to determine the Eb, TDOS, and partial density of states (PDOS). Additionally, CDD analysis was performed with the Dmol3 program package to confirm the electronic redistribution upon ion binding.

Membrane depolarization assay

The impact of the compounds on membrane depolarization was assessed using the fluorescent dye $DiSC_3(5)$ (Sigma-Aldrich, USA). An overnight culture of *P. aeruginosa* 541 was prepared, washed, and resuspended in deionized water (pH 7.0). The cell suspension was adjusted to an OD_{600} of 0.37. For staining, the bacterial suspension (1 mL) was mixed with 2 μL of 1 mg/mL $DiSC_3(5)$ at 37°C for 15 min in the dark. Fifty microliters of the stained suspension were transferred to a black 96-well plate. The initial fluorescence was measured at 9 s intervals for 15 min using a Spectra MAX iD3 microplate reader (excitation/emission = 620/670 nm).[61] Subsequently, 30 μL of compound at 8× MIC was added to the wells, and fluorescence readings were continued for an additional 15 min. Melittin and DMSO served as controls. All the assays were conducted in triplicate for consistency and reliability.

Membrane integrity assay

PI (Sigma–Aldrich, USA), a dye known to stain nuclear chromatin following cell membrane disruption, was used to evaluate the ability of the tested compounds to compromise cytoplasmic membrane integrity. *P. aeruginosa* 541 cells were washed and resuspended in deionized water (pH 7.0), and the OD_{600} was adjusted to 1.0. A bacterial suspension (30 μL) was mixed with 20 μM PI at 37°C for 10 min in the dark.[62] Fluorescence readings were taken at excitation/emission wavelengths of 535/615 nm using a Spectra MAX iD3 microplate reader, with measurements recorded at 9 s intervals. After a 15 min period, each test compound (30 μL), adjusted to a final concentration of 8× MIC, was added to the wells, and the fluorescence was monitored immediately for 15 min. Melittin and DMSO were used as controls. All the experiments were performed in triplicate to ensure reliability.

DNA damage assay

P. aeruginosa 541 in the exponential growth phase was mixed with fresh LB medium at a ratio of 1:1, and solutions of each tested compound were added at a final concentration of 8× MIC. The mixture was cultured at 37°C and 120 rpm for 12 h, 16 h, or 20 h. At each time point, the bacterial culture was centrifuged, and the cells were resuspended in sterile water. DAPI at a final concentration of 20 μg/mL was added to the resuspension and mixed in a black 96-well plate in the dark. The fluorescence values were then immediately measured at excitation/emission wavelengths of 364/454 nm using a Spectra MAX iD3 microplate reader. The bacterial cells for each test compound were cultured for 12 h and then retrieved. After DAPI staining, the slides were prepared and observed under an ECLIPSE Ts2-FL microscope (Nikon, Japan). DMSO served as the negative control, and all the experiments were conducted with three independent replicates.

SEM assay

P. aeruginosa 541 in the exponential growth stage was treated with the drug combination (8× MIC) at 37°C for 0 h, 2 h, and 4 h. At each time point, 2 mL of the culture was collected, centrifuged, and fixed with 2.5% glutaraldehyde solution for 2 h. The samples were then washed and resuspended in deionized water. Sequential dehydration was performed using 30–90% ethanol for 10 min each, followed by three rounds of dehydration with absolute ethanol for 30 min. The samples were air-dried, attached to conductive tape, coated with gold, and analyzed by SEM (GeminiSEM 500, Carl Zeiss).

TEM assay

P. aeruginosa 541 in the exponential growth stage was treated with the drug combination (8× MIC) at 37°C for 0 h, 2 h, and 4 h. At each time point, 2 mL of the culture was collected, centrifuged, and fixed overnight in glutaraldehyde solution, fixed in 1% osmium acid solution for 2 h, rinsed in phosphate buffer for 15 min, and dehydrated with an ethanol gradient for 30 min, followed by pure ethanol, ethanol:acetone (1:1) and pure acetone twice. The treated samples were embedded and polymerized, and ultrathin sections were prepared. The sections were stained with lead citrate solution and a solution of uranyl acetate saturated in 50% ethanol, followed by rinsing with distilled water, and observed using TEM (HT7700 EXALENS, Hitachi).

ROS detection

P. aeruginosa 541 in the exponential growth phase was adjusted to OD_{600} = 0.5, each test compound solution was added at 8× MIC, the mixture was cultured at 37°C for 2 h,[62] and 1 mL of the bacterial culture was sampled from each group and then centrifuged at 3000 rpm and 4°C for 10 min to collect the precipitate. The ROS content in each group was determined via the Bacterial Oxidative Stress Reactive Oxygen Fluorescence Assay Kit (JIWEI, China).

Comet assay

An overnight culture of *P. aeruginosa* 541 was combined with fresh LB medium at a 1:1 ratio, followed by the addition of compounds to achieve a final concentration of 8× MIC. The cultures were incubated at 37°C and 120 rpm for 12 h). The bacterial suspensions were collected for subsequent analysis. DNA damage was assessed by using a bacterial DNA damage comet assay kit (GENMED, USA), and the results were visualized with an ECLIPSE Ts2-FL system (Nikon, Japan) and analyzed by DNA damage was assessed using the Bacterial DNA Damage Comet Assay Kit (GENMED, USA), and the results were visualized with an ECLIPSE Ts2-FL system (Nikon, Japan) and analyzed with the Comet Assay Software Project (CASP).

ATP detection

P. aeruginosa 541 in the exponential growth phase was adjusted to an OD_{600} of 0.5. Test compound solutions were added at a final concentration of 8× MIC, and the mixtures were incubated for 2 h at 37°C.[63] Then, 3 mL of bacterial culture was collected from each group and centrifuged (8000 rpm, 4°C, 5 min) to obtain the precipitate. The pellet was subsequently resuspended in sterile water (1:1 dilution) and disrupted via ultrasonication. The samples were then boiled at 100°C for 5 min, followed by centrifugation at 8000×g and 4°C for 15 min, and the supernatant was collected for further analysis. The ATP levels in the supernatant were measured using a Micro ATP Content Detection Kit (Abbkine, China), and the protein concentration was measured via a BCA Kit (Beyotime, China).

Antibiofilm activity of *P. aeruginosa in vitro*

One milliliter of *P. aeruginosa* 541 (1×10^{-7} CFU) was added to a 0.15 mm confocal dish.[64] A final concentration of 4× MIC of **7**+bismuth citrate was introduced, with equal doses of single agents and solvent serving as negative controls. The culture was incubated for 24 h at 37°C. The samples were then washed slowly with deionized water. The biofilm was then stained with two fluorescent dyes, namely, DAPI and PI. Confocal laser scanning microscopy (Leica STELLARIS 5, Germany) was employed for fluorescence imaging to evaluate the effects of the compounds on biofilm formation.

Proteomic analysis

P. aeruginosa 541 in the exponential growth phase was combined with fresh LB medium at a 1:1 ratio. Solutions containing a mixture of bismuth citrate and compound **7** were added at final concentrations of 8× MIC (128 μg/mL bismuth citrate +8 μg/mL **7**) or 16× MIC (256 μg/mL bismuth citrate +16 μg/mL **7**). Compound **7** (8 μg/mL) was also added alone, and a blank control group without any drug treatment was established. The cultures were incubated at 37°C and 120 rpm for 12 h. Following incubation, bacterial precipitates were collected via centrifugation and prepared for proteomic analysis. Each condition was analyzed in biological triplicate. Total protein was extracted from bacterial samples stored at −80°C.[65] The concentration and quality of the extracted proteins were evaluated using the Bradford protein quantification kit and 12% SDS-PAGE gel electrophoresis. Proteins meeting the required standards were subjected to enzymatic hydrolysis with trypsin.[66] Salt was removed using a C18 column, and the collected solution was filtered and freeze-dried for future use. The samples were analyzed with the Vanquish *Neo* UPLC–Astral LC/MS DIA method, and the data were processed as follows. Functional annotation was achieved through Gene Ontology (GO) and InterPro-based (IPR) analyses, which were performed using InterProScan against a nonredundant protein database, which includes PANTHER, Pfam, ProSite, PRINTS, SMART, and ProDom.[67] Additionally, the Clusters of Orthologous Groups (COG) and KEGG databases were used to explore protein families and pathways. Differentially expressed proteins (DEPs) were analyzed via volcano plot generation, cluster heatmaps, and GO, IPR, and KEGG enrichment analyses.[68]

Potassium ion assay

P. aeruginosa 541 cultured overnight was adjusted to an OD_{600} of 0.5 and mixed with fresh LB medium at a 1:1 ratio, followed by the addition of compounds to achieve a final concentration of 8× MIC. A liquid culture of the bacterial group without compound was used as blank control. The cultures were incubated at 37°C with shaking at 120 rpm for 12 h. Bacterial suspensions were collected

for subsequent analysis. The K^+ concentration was quantified using the bacterial potassium ion concentration chemical colorimetric quantitative detection kit (GENMED, USA) following the manufacturer's protocol.

Fluorescence-based evaluation of compound–DNA interaction

Genomic DNA (gDNA) was extracted from *P. aeruginosa* 541 with the TIANamp bacteria DNA kit (TIANGEN, China) and dissolved in 10 mM Tris-HCl buffer (pH 7.2). gDNA (40 μg/mL) was preincubated with 2 μg/mL DAPI for 2 min to form a complex. Aliquots of 100 μL of the complex were transferred to a black 96-well plate. The **7**–bismuth citrate complex was then added to achieve different concentrations (0–32× MIC), with the total volume in each well brought to 200 μL with Tris-HCl buffer. Compound **7** and bismuth citrate were also used alone as controls. The plate was incubated in the dark at room temperature for 15 min before fluorescence measurement. The emission spectrum (360–650 nm) was recorded following excitation at 320 nm. The net fluorescence intensity of each sample of each sample was determined by subtracting the measured signal of the sample from that of the corresponding drug-only control.

SPR study

Samples were diluted to the printing concentration and used as the printing working solution. The working solution was then printed onto a 3D photocrosslinked chip by using a Biodot AD1520 printer (Biodot, USA). The chip was then vacuum-dried and subjected to photocrosslinking. The chip was then sequentially washed with DMF, C_2H_5OH, and H_2O for 15 min each, blown dry with nitrogen, and assembled with a flow cell cover. PBST (0.1% Tween 20) was added to the stock solutions of the compound samples, which were subsequently diluted to five concentrations ranging from 10 nM to 2560 nM. All samples were tested with PBST serving as the flow medium throughout the experiment. An SPR assay was conducted on a bScreen LB 991 label-free microarray system (Berthold, Germany) following the manufacturer's protocol.

In vivo antibacterial activity assessment in lung infection model

Six-week-old female SPF ICR mice (20–22 g) were allowed to acclimatize over a 12 h light/dark cycle for 6 days. Cyclophosphamide at 150 mg/kg and 100 mg/kg was administered via intraperitoneal injection for 4 days and 1 day, respectively, to generate neutropenic mice. *P. aeruginosa* 541 was cultured with shaking overnight at 37°C and 220 rpm. Each mouse was infected with $\sim10^7$ *P. aeruginosa* 541 cells via the nasal cavity. Two hours after infection, the mice were treated with ciprofloxacin (5 mg/kg), bismuth citrate (5 mg/kg), bismuth citrate (5 mg/kg), compound **7** (5 mg/kg), a combination of bismuth citrate (5 mg/kg) and compound **7** (2 mg/kg), a combination of bismuth citrate (5 mg/kg) and compound **7** (5 mg/kg), a combination of bismuth citrate (8 mg/kg) and compound **7** (8 mg/kg), a combination of bismuth citrate (32 mg/kg) and compound **7** (32 mg/kg) via intraperitoneal injection. The control mice were injected with saline solution. A second dose was given after 12 h. At 24 h post-treatment, the mice were euthanized. Lung, heart, liver, spleen, and kidney tissue samples and blood samples were collected. Lung homogenates were plated on LB medium as serial dilutions. The bacterial concentration was recorded as CFU/g, and the serum biochemical indicators were evaluated by automated biochemical analysis. H&E staining was performed on the heart, liver, spleen, and kidneys.

The pretreatment of the mice is described above. Each mouse was infected with $\sim10^7$ *P. aeruginosa* 535 cells via the nasal cavity. Two hours after infection, the mice were treated with ciprofloxacin (16 mg/kg), bismuth citrate (8 mg/kg), compound **7** (8 mg/kg) or a combination of bismuth citrate (8 mg/kg) or compound **7** (8 mg/kg) via intraperitoneal injection. The control mice were injected with saline solution. A second dose was given after 12 h. At 24 h post-treatment, the mice were euthanized. The lungs were collected. Lung homogenates were plated on LB medium as serial dilutions. The bacterial concentration was recorded as CFU/g.

In vivo antibacterial activity assessment in a biofilm-associated wound colonization

PDMS sheets (0.1 × 0.5 cm^2) were fabricated following the recommended protocol for the Sylgard 184 Silicone Elastomer Kit (Dow Corning, USA). Subsequently, biofilms were allowed to form on the PDMS sheets. Female BALB/c mice (4–6 weeks) weighing 18–20 g were anesthetized via intraperitoneal injection of 1.25% bromethol at a dosage of 12 mL/kg 15 min prior to surgery. The dorsal area of each mouse was then depilated using depilatory paste and disinfected by wiping with 75% ethanol. An ~0.5 cm incision was made on the back, and PDMS sheets precoated with *P. aeruginosa* 7034 biofilms were implanted subcutaneously at the incision site. The surgical wound was then closed with sutures. Twenty-four hours post-implantation, the mice were administered daily *in situ* injections of ciprofloxacin (16 mg/kg), tobramycin (16 mg/kg), bismuth citrate (8 mg/kg), compound **7** (8 mg/kg), or a combination of bismuth citrate (8 mg/kg) and compound **7** (8 mg/kg). The mice in the control group received saline injections instead. The appearance of the surgical wounds was documented daily through photography. At 96 h post-implantation, the mice were humanely sacrificed. All the PMDS sheets were transferred to 0.5 mL of sterile PBS. Following 15 min of vortex mixing to disperse the bacteria, the bacterial suspension was serially diluted to an appropriate concentration and plated onto LB agar plates. After incubation at 37°C for 16 h, the colonies of *P. aeruginosa* 7034 were counted. The skin and muscle tissues of the mice were fixed in 4% paraformaldehyde solution, and tissue pathology was evaluated via H&E staining.

Mouse survival rate

A mouse model of neutropenic lung infection (10 female mice per group) was established via the specific steps described above. *P. aeruginosa* was cultured overnight at 37°C and 220 rpm. Each mouse was infected with $\sim10^7$ *P. aeruginosa* cells via the nasal cavity. Two hours after infection, the mice were treated with ciprofloxacin (5 mg/kg), bismuth citrate (5 mg/kg), compound

7 (5 mg/kg), or a combination of bismuth citrate (5 mg/kg) or compound **7** (5 mg/kg) via intraperitoneal injection. The control mice were injected with saline solution. A second dose was given after 12 h. Mouse survival was monitored until the end of the experiment.

In vivo safety evaluation

All the mouse studies were conducted with SPF ICR mice (20–22 g). The mice were housed with a 12 h light/dark cycle for 6 days at 22°C–25°C. The mice were randomly divided into four groups, including a control group (10 mice/group, equal numbers of males and females). The mice in the treatment groups were treated with compound **7** at 2, 8 or 16 mg/kg, while the control group received 5% DMSO/95% saline. Compound **7** was administered via intraperitoneal injection for 28 consecutive days. During this period, the mice were monitored for toxicity and clinical toxicology symptoms daily, and their body weights were recorded. The mice were euthanized after the 28-day treatment period. Blood samples were collected and analyzed for hematological parameters using an automated hematology analyzer, whereas serum biochemical indicators (ALT, AST, BUN, CR) were measured using an automated biochemical analyzer. Cecal contents were collected, and 16S rRNA high-throughput sequencing technology was used to analyze the composition and diversity of the gut microbiota. The injection sites were dissected, and tissue damage was recorded. The heart, liver, spleen, lungs, and kidneys were collected. H&E staining was performed on the collected organs.

The relative organ weight was determined via the following formula:

Relative organ weight (mg/g) = Organ weight/Body weight.

QUANTIFICATION AND STATISTICAL ANALYSIS

Statistical data were analyzed using GraphPad Prism or SPSS software. Detailed statistical information for each experiment is provided in the figure legends. Mean ± standard error of the mean (error bars) is shown. A p value of less than 0.05 was considered statistically significant. p values are indicated as follows: no significance (ns) $p > 0.05$, $^{*}p < 0.05$, $^{**}p < 0.01$, $^{***}p < 0.001$ and $^{****}p < 0.0001$.